

**Pool stratification and mixing induced by steam injection through spargers:
analysis of the PPOOLEX and PANDA experiments**

Gallego-Marcos Ignacio, Kudinov Pavel, Villanueva Walter, Kapulla Ralf,
Paranjape Sidharth, Paladino Domenico, Laine Jani, Puustinen Markku, Räsänen
Antti, Pyy Lauri, Kotro Eetu

This is a Final draft version of a publication
published by Elsevier
in Nuclear Engineering and Design

DOI: 10.1016/j.nucengdes.2018.07.004

Copyright of the original publication: © 2018 Elsevier B.V.

Please cite the publication as follows:

Gallego-Marcos, I., Kudinov, P., Villanueva, W., Kapulla, R., Paranjape, S., Paladino, D., Laine, J., Puustinen, M., Räsänen, A., Pyy, L., Kotro, E. (2018). Pool stratification and mixing induced by steam injection through spargers: analysis of the PPOOLEX and PANDA experiments. Nuclear Engineering and Design, vol. 337, pp. 300-316. DOI: 10.1016/j.nucengdes.2018.07.004

**This is a parallel published version of an original publication.
This version can differ from the original published article.**

Pool Stratification and Mixing Induced by Steam Injection through Spargers: Analysis of the PPOOLEX and PANDA experiments

Ignacio Gallego-Marcos^a, Pavel Kudinov^a, Walter Villanueva^b, Ralf Kapulla^c, Sidharth Paranjape^c, Domenico Paladino^c, Jani Laine^d, Markku Puustinen^d, Antti Räsänen^d, Lauri Pyy^d, Eetu Kotro^d

^aRoyal Institute of Technology (KTH), Division of Nuclear Engineering, Stockholm, Sweden.

^bRoyal Institute of Technology (KTH), Division of Nuclear Power Safety, Stockholm, Sweden.

^cPaul Scherrer Institute (PSI), Division of Nuclear Energy and Safety Research, Villigen, Switzerland

^dLappeenranta University of Technology (LUT), Unit of Nuclear Safety Research, Lappeenranta, Finland

E-mails: igm@kth.se, pkudinov@kth.se, walterv@kth.se, ralf.kapulla@psi.ch,

sidharth.paranjape@psi.ch, domenico.paladino@psi.ch, jani.laine@lut.fi, markku.puustinen@lut.fi,

antti.rasanen@lut.fi, lauri.pyy@lut.fi, eetu.kotro@lut.fi

ABSTRACT

Spargers are multi-hole injection pipes used in Boiling Water Reactors (BWR) and Advanced Pressurized (AP) reactors to condense steam in large water pools. A steam injection induces heat, momentum and mass sources that depend on the steam injection conditions and can result in thermal stratification or mixing of the pool. Thermal stratification reduces the steam condensation capacity of the pool, increases the pool surface temperature and thus the containment pressure. Development of models with predictive capabilities requires the understanding of basic phenomena that govern the behavior of the complex multi-scale system. The goals of this work are (i) to analyze and interpret the experiments on steam injection into a pool through spargers performed in the large-scale facilities of PPOOLEX and PANDA, and (ii) to discuss possible modelling approaches for the observed phenomena. A scaling approach was developed to address the most important physical phenomena and regimes relevant to prototypic plant conditions. The focus of the tests was on the low steam mass flux and oscillatory bubble condensation regimes, which are expected during a long-term steam injection transient, e.g. in the case of a Station Black Out (SBO). Exploratory tests were also done for chugging and stable jet conditions. The results showed a similar behavior in PPOOLEX and PANDA in terms of jet induced by steam condensation, pool stratification, and development of hot layer and erosion of the cold one. A correlation using the Richardson number is proposed to model the erosion rate of the cold layer as a function of the pool dimensions and steam injection conditions.

KEYWORDS

Pool stratification, oscillatory bubble, thermocline erosion, Richardson, turbulence, chugging

HIGHLIGHTS

- Pool stratification and mixing phenomena studied in different scale facilities
- Formation of hot and cold layers at low steam injections through spargers
- New Richardson number based correlation for the erosion rate of the cold layer
- Multi-hole steam injection induced self-similar downward inclined jets
- Chugging is suppressed at pool temperatures higher than 65 °C

NOMENCLATURE

A	Area, Amplitude
B	Jet central velocity decay rate
C	Coefficient
C_D	Discharge coefficient
D	Vertical distance from the sparger injection centerline to the thermocline
d	Injection hole diameter
f	Frequency
G	Mass flux
g	Gravitational acceleration
I	Turbulent intensity
K	Constant for jet spread rate
k	Turbulent kinetic energy
k_n	n^{th} root of the derivative of the first order Bessel function $J_1'(k_n)$
L_H	Vertical turbulent eddy length scale
M	Momentum
m	Mass
\dot{m}	Mass flow rate
N	Number of samples in PIV
n	Constant
P	Pressure
R	Radius
Ri	Richardson number
r	Radial distance
T	Temperature
U	Mean flow velocity
U_E	Erosion velocity in vertical direction
u_H	Vertical turbulent eddy velocity
u'	Fluctuating turbulent velocity
x	Axial distance
z	Vertical distance
Δb	Buoyancy jump, equivalent to g'
Greek symbols	
α	Injection angle
γ	Heat capacity ratio
τ	Shear stress
π	Pi number
ρ	Density
ω	Time scale
Subscripts	

0	Jet centerline
1	Inside the sparger
2	Injection holes outlet
<i>c</i>	Cold layer
<i>crit</i>	Critical flow conditions
<i>E</i>	Energy
<i>exp</i>	Experimental
<i>h</i>	Hot layer
<i>i</i>	Injection holes, tensor index
<i>L</i>	Liquid
<i>M</i>	Mass
<i>p</i>	Pool
<i>P</i>	Momentum
<i>r</i>	Rings of holes in the sparger
<i>s</i>	Steam, shear
<i>sf</i>	Shear-free
<i>sp</i>	Sparger
<i>tc</i>	Thermocline
<i>th</i>	Theoretical
∞	Downstream of location 2
\sim	Non-dimensional quantity
Acronyms	
ADS	Automatic Depressurization System
AP	Advanced Pressurized
BWR	Boiling Water Reactor
CFD	Computational Fluid Dynamics
DCC	Direct Contact Condensation
EHS/EMS	Effective Heat/Momentum Source
FFT	Fast Fourier Transform
IRWST	In-containment Refuelling Water Storage Tank
LES	Large-Eddy Simulation
LRR	Load Reduction Ring
PIV	Particle Image Velocimetry
PSP	Pressure Suppression Pool
RANS	Reynolds-Averaged Navier-Stokes
SBO	Station Black-Out
SRV	Safety Relief Valve
TC	ThermoCouple

1. INTRODUCTION

Steam condensation in a large water pool is used in some designs of light water reactors to prevent containment over-pressure [1]. In Boiling Water Reactors (BWR) this pool is known as the Pressure

Suppression Pool (PSP), whereas in Generation III reactors such as the AP1000 and APR1400 the pool is known as the In-containment Refuelling Water Storage Tank (IRWST). In a BWR, steam can be injected into the PSP (in case of loss of coolant accident) through large diameter blowdown pipes connected to the drywell, or small-diameter multi-hole spargers used for controlled depressurization of the primary coolant circuit.

The development of thermal stratification in the pool is of safety concern since it leads to higher pool surface temperatures, and thus higher containment pressures, compared with completely mixed pool conditions. An example of such behavior can be observed in the Fukushima Daiichi Unit 3 accident, during the operation of the Reactor Core Isolation Condenser (RCIC) [2, 3]. Lumped parameter codes under-estimated the maximum pressure by about 160 kPa when assuming mixed pool conditions, whereas a much better agreement was obtained assuming pool stratification [4].

To enable prediction of thermal stratification and mixing induced by steam injection into a subcooled pool, Li & Kudinov (2010) [5] introduced the concepts of the Effective Heat Source (EHS) and Effective Momentum Source (EMS) models. The premise of these models is that due to the difference in spatial and time scales between direct contact condensation (DCC) phenomena and large pool behavior, only the integral effects of the DCC phenomena on the pool should be modeled. These effects are defined as heat and momentum sources, which determine the large-scale pool circulation and temperature distribution.

Experimental data is necessary to understand which characteristics of small-scale phenomena affect the effective heat and momentum sources. For example, analysis of the PPOOLEX experiments with blowdown pipes showed that the momentum source induced by chugging regime can be determined by the frequency and amplitude of the liquid level oscillations inside the pipe using a synthetic jet model [6, 7]. Further development of the models was done to scale the frequency and amplitude, allowing the code to predict the momentum source based on the time dependent injection conditions and geometry of the system [8]. Validation of the EHS/EMS models against a large set of experiments performed in the PPOOLEX facility showed very good agreement with the pool temperature and containment pressures [9, 10].

In this paper, we address a set of conditions and respective phenomena related to a steam injection through spargers and its effect on the pool, e.g. compared to the previous analysis done for blowdown pipes, we consider smaller injection holes, the multi-hole injection parallel to the thermocline, etc.

Previous experiments on single-hole steam injection showed that the most important variables determining the steam condensation regime are the steam mass flux, pool subcooling, and injection hole diameter [11]. Based on these variables, correlations were proposed for the penetration length, heat transfer coefficient, pressure pulses, etc. [12, 13]. Condensation regime maps for sonic and sub-sonic steam injections were proposed by Wu et al. [14] and Chan & Lee [15], respectively. Other regime maps such as the ones from Aya & Nariai [16] included the effect of a drywell.

The effect of steam injections through a single-hole sparger into a water pool were studied in [17, 18] using small-scale facilities. Thermal stratification was reported at conditions relevant to RCIC injection in a BWR. In [17], the pressure in the wetwell gas space was observed to have an effect on the development of stratification, being stronger in the pressurized cases.

The possibility of thermal stratification development was further confirmed in [19] using a multi-hole sparger injection through a scaled down IRWST sparger of the AP1000. Similar to [18], the Richardson number (ratio between buoyant and inertia forces) was found to determine the transition between stratification and mixing of the pool. Vertical spargers were used in [20] to obtain data for further

development of the steam condensation region approach proposed in [21], validated against complete mixing transients.

The chugging regime was studied experimentally by Gregu et al. in [22], where different modes of condensation were identified and classified in a regime map. Thermal stratification and mixing during the chugging regime in blowdown pipes were also studied by Laine et al. in [23]. The data from these experiments was used for the development and validation of the EHS/EMS models [6, 7, 8, 9, 10].

A notable work was done by Fernando et al. [24, 25] describing the different mechanisms which can erode a stable stratified layer. Fernando et al. [26] and other researchers [27, 28] also demonstrated that the bulk Richardson number can be used to determine the erosion mode and, most importantly, the erosion velocity. Previous pool analysis with the Richardson number were mainly focused on the boundary between mixing and stratification [19, 29], whereas the results from [26] allow predicting the transition between these states.

Even though important separate phenomena related to spargers and pool are addressed in the literature, most of the experiments do not address the effect of steam injection conditions on the pool response.

Model development and validation for safety analysis require (i) separate effect tests that address key phenomenon separately to enable model calibration; (ii) integral effect tests with gradually increasing number of interplaying phenomena to enable code validation. Prototypic scenarios are considered in the selection of the relevant conditions and regimes that should be provided in the design of the separate and integral effect tests. Yet, reproducing an accident scenario is not a goal since the test results cannot be scaled-up directly in a general case.

The goals of this work are (i) to analyze and interpret the experimental results from the pool test with sparger performed in the PPOOLEX (LUT, Finland) [30] and PANDA (PSI, Switzerland) [31] facilities and (ii) to discuss possible modelling approaches for the observed phenomena. The tests were designed to investigate the large-scale temperature and velocity fields induced by the steam injection, which can be used to develop and validate EHS/EMS modelling approaches implemented in CFD. Micro-scale phenomena related to bubble or jet dynamics requires smaller-scale facilities, such as the Separate Effect Facility (SEF) built at LUT, Finland, which is a subject of the future work.

2. SCALING OF THE PPOOLEX AND PANDA EXPERIMENTS WITH SPARGER

The PPOOLEX and PANDA facilities were originally designed to study the containment thermal-hydraulics of a BWR and a European Simplified BWR (ESBWR) respectively. PPOOLEX consists of a single stainless steel vessel divided into a drywell and wetwell, and a steam generator of 1 MW capacity. PANDA is divided into 2 drywells and 2 wetwell vessels, and has a steam generator of 1.5 MW. The wetwell vessel of the PANDA facility has roughly double the height and diameter compared with the PPOOLEX facility (Figure 1).

The sparger experiments were scaled to preserve ranges of parameters and regimes that determine most important physical phenomena appearing in plant scale. Since not all phenomena can be preserved simultaneously in a large, but still reduced scale facility such as PPOOLEX or PANDA, the experimental data cannot be directly extrapolated to plant conditions. Instead, it will be used for analysis of the physical phenomena and code development, which, once validated, can be applied to predict plant behavior.

The roadmap to scaling proposed by D'Auria & Galassi [32] was followed in the design of the tests. The BWR Mark II plant, and the Station Black Out (SBO) scenario with steam discharge into the suppression pool through 32 spargers were considered. Simulations of such scenario were done with the GOTHIC

code [33], and the results are presented in Table 1. At 500 s, the steam mass flux at the injection holes is $\sim 200 \text{ kg}/(\text{m}^2\text{s})$, indicating that sub-sonic condensation regimes are expected during most of the transient. The phenomena of safety importance are the development of thermal stratification and the time needed to restore the complete pressure suppression capacity of the pool by slow erosion or fast mixing of the stratified layers.

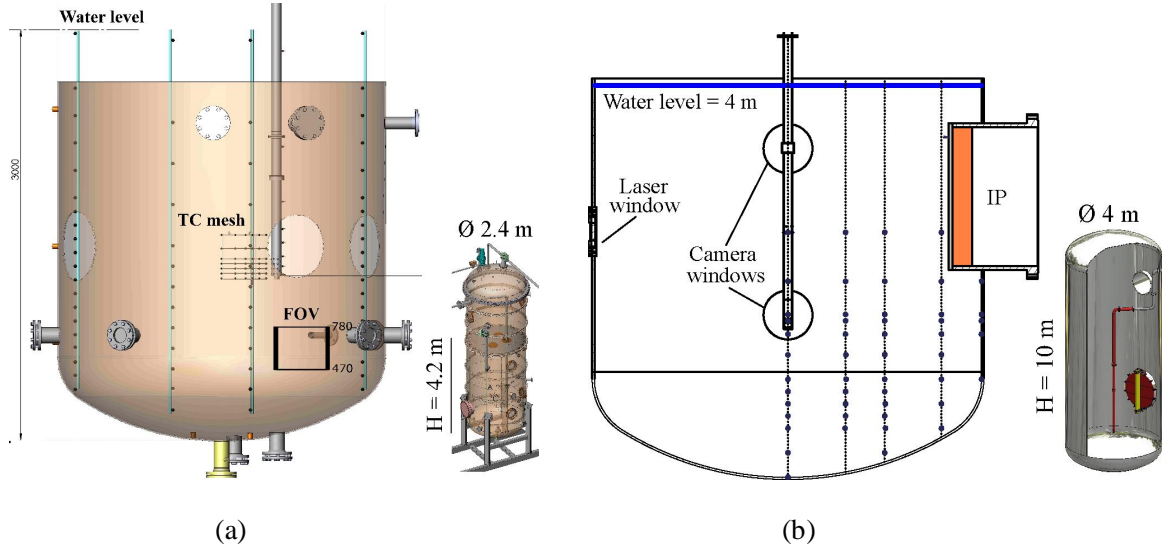


Figure 1: Over-view of the pool test sections in (a) PPOOLEX and (b) PANDA facilities during the experiments with sparger.

ABB-Atom design of spargers for BWR Mark-II and III plants was considered in the scaling process: upper ring of downward facing holes, known as the Load Reduction Ring (LRR), and radially outwards holes at the sparger head [20]. Other designs, such as the BWR Mark I by General Electric [34] and AP1000 by Westinghouse [19], use T-quenchers, which inject steam through horizontal sections of the sparger pipes with a wide range of injection hole diameters.

Table 1: Steam injection conditions during a BWR transient where 8 safety relief valves are activated and kept open.

Time after SRVs activation	Steam pressure at the sparger inlet	Steam mass flow through all spargers	Steam mass flux through sparger pipe ^a	Steam mass flux through injection holes ^a
300 s	400 kPa	140 kg/s	250 $\text{kg}/(\text{m}^2\text{s})$	430 $\text{kg}/(\text{m}^2\text{s})$
500 s	240 kPa	66 kg/s	115 $\text{kg}/(\text{m}^2\text{s})$	200 $\text{kg}/(\text{m}^2\text{s})$
10000 s	190 kPa	20 kg/s	35 $\text{kg}/(\text{m}^2\text{s})$	60 $\text{kg}/(\text{m}^2\text{s})$

^a Assuming a total of 32 spargers, each with a pipe diameter of 150 mm and an injection hole area of 10100 mm^2

Once the plant design and transient are selected, the experimental design and conditions can be defined to study relevant phenomena at the macro, meso, and micro scales. According to [32] the macro scales are best preserved when using a full-length and time-preserving facility. This could not be achieved due to geometrical and power constraints of PPOOLEX and PANDA. Nevertheless, the maximum possible pool depth was used, and characteristic time scale ratios of mass, momentum, and energy of the steam injected into the pool [21] were preserved. In the micro scale, Li et al. [35] and Sonin [36] emphasize that two-phase flow phenomena occurring at the steam jets cannot be properly scaled. Therefore, the dimensions of

the injection holes, mass flux, and thermo-physical properties of the fluids were kept as close as possible to the prototypic ones. Further details of the design parameters selected for the macro, meso, and micro scales are given below. The final design of the PPOOLEX and PANDA spargers are presented in Figure 2 and Table 3.

Macro scale (water pool): to preserve typical ratios of spatial and temporal scales and determine dimensions of the pool; location of the injection in the pool; ratio of energy and momentum rates.

(1) The total height of the PPOOLEX wetwell is 4.2 m. The pool depth was set to 3 m in order to maintain a sufficient gas volume allowing for a rise of the liquid level during the experiment. PANDA pool depth was set to 4 m due to geometrical constraints imposed by the upper inter-connecting pipe. With these dimensions, the depth to diameter ratio of the water pool was about 0.7-1 for both facilities. In a Nordic BWR, the ratio of pool depth to the minimum lateral scale is about 1.5-2 [1]. On the other hand, the ratio for the largest horizontal length scale will tend to much lower values (~0.4).

(2) To obtain a similar ratio of cold layer thickness to pool depth, the sparger submergence ratio was set to the prototypical 70% value found in Nordic BWRs [37]. However, further experiments might consider preserving the actual distance between the sparger and pool bottom. Such arrangement would enable a better understanding on the relation between erosion velocity and distance between the sparger and interface between stratified layers.

(3) In PPOOLEX, the sparger was located closer to the wall, whereas in PANDA it was located at the center of the pool. These two configurations are expected to be representative of the different locations where the sparger can be found in the BWR pool.

(4) Given the limitations in steam flow generation, the total injection hole area was selected such that the steam mass fluxes fall within 0-150 kg/(m²s), which corresponds to the expected fluxes past ~500 s after SRVs activation (Table 1). With the injection hole area the time scales of mass ω_M , momentum ω_P , and energy ω_E were calculated with equations (1) using the data from Table 1. The results are presented in Table 2, where we can see that the order of magnitude for the time scales are well preserved.

$$\omega_M = \frac{\dot{m}_S}{m_L}; \quad \omega_P = \frac{\dot{m}_S v_S}{m_L \sqrt{g z_p}}; \quad \omega_E = \frac{\dot{m}_S h_S}{m_L h_L} \quad (1)$$

Table 2: Mass, momentum, and energy time scales compared to prototypical BWR conditions 500 s after the activation of 8 Safety Relief Valves. The steam mass flow used for PPOOLEX and PANDA was the maximum allowed by steam generator of the facilities: 0.27 kg/s and 0.37 kg/s, respectively. Steam was assumed to be injected at saturated 150 kPa conditions in all cases.

Time scales [s ⁻¹]	BWR	PPOOLEX	PANDA
Mass	[2.0 – 3.3] e-5	2.1 e-5	8.2e-6
Momentum	[3.7 – 8.1] e-4	6.0 e-4	1.8 e-4
Energy	[6.7 – 10.6] e-4	6.6 e-4	2.6 e-4

Meso scale (sparger pipe): to determine design parameters of the sparger pipe that provide relevant regimes for the phenomena such as condensation and condensation at the pipe surface.

(1) The sparger pipe diameter was designed to preserve the steam mass fluxes presented in Table 1, which is one of the major variables determining the condensation regime inside the pipe [38]. Wall thickness of the pipe was set to a prototypic value of 4 mm.

(2) The LRR section was designed with a diameter 70 % larger than the sparger pipe. The distance between the LRR and the sparger end was set to 50 % of the submergence, similar to the 30 to 50 % range found in prototypic design.

Micro-scale (injection holes): to determine design parameters affecting direct contact condensation phenomena.

(1) Similar to prototypic sparger designs [20], the injection hole area was distributed between the LRR and the sparger head in a 20 to 80 % ratio, respectively.

(2) The injection hole diameters were 8 and 9.5 mm, approaching to the prototypic values of 10-12 mm. The number of holes and diameters were selected to provide close to prototypic horizontal and vertical pitch (which affect the interaction between neighboring jets), while preserving the injection hole area needed to reach the steam mass fluxes from Table 1. Similar to the spargers found in BWRs, the injection holes were chamfered at the outlet with $\phi 16 \times 120^\circ$ and $\phi 19 \times 120^\circ$ for PPOOLEX and PANDA, respectively. Further designs might consider preserving the total number of holes per ring to maintain the angle between jets in their axial direction.

(3) The ratio between the injection hole area and sparger cross section area, about 0.55 in a BWR, was also preserved in the scaled models. This ratio is an important parameter since it is one of the major contributors to the pressure drop across the injection holes, which affects the mass flow distribution between them.

Table 3: Dimensions of the PPOOLEX and PANDA sparger experiments compared to prototypical BWR

	BWR ^a	PPOOLEX	PANDA
Pool volume	2000-3300 m ³	13 m ³	45 m ³
Pool depth	6-11 m	3 m	4 m
Pool diameter ^b	11-14/22-25 m	2.4 m	4 m
Submergence ratio	70 %	70 %	70 %
Sparger pipe diameter	150 mm	68 mm	81 mm
Injection holes diameter	10-12 mm	8 mm	9.5 mm
Total injection hole area	10100 mm ²	2010 mm ²	2800 mm ²
Horizontal pitch to diameter	3.6	3.3	3.3
Vertical pitch to diameter	4.5	4.5	4.5

^a Approximate values based on available data

^b Values of the BWR correspond to the inner/outer diameters of the annular pool

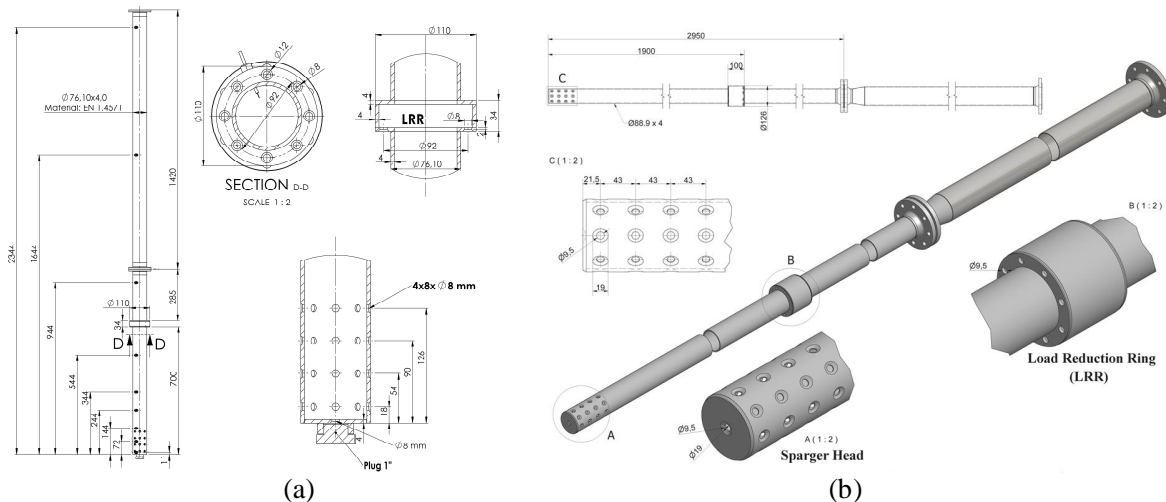


Figure 2: Sparger design obtained with the scaling and used in the (a) PPOOLEX and (b) PANDA tests.

2.1. Instrumentation

In PPOOLEX and PANDA, the steam injection conditions of mass flow, pressure, and temperature were measured about 5 m above the injection holes. Since the steam temperature was expected to change along

the submerged section of the sparger, several TCs were also located along the pipe, reaching until the injection holes. The liquid level in the pool, used to cross-check the mass flow injected into the pool, was computed by the difference between a pressure measurement in the gas space and another one inside the pool.

A total of 68 and 62 K-Type TCs with an average error of ± 2 °C and recording frequencies of 0.67 and 0.5 Hz were used in the water pool of the PPOOLEX and PANDA facilities, respectively. The TCs were arranged in vertical trains to capture the pool temperature profile at different locations, Figure 1. Due to the large temperature gradients expected to occur at the thermocline, a higher vertical resolution of about 150 mm was used below the sparger injection. Above the sparger, where a homogeneously mixed flow is expected, this resolution was increased to about 300 mm. In PPOOLEX, 42 K-Type TCs capable of recording temperatures with 20 Hz were arranged into a so called TC mesh in front of the sparger, aligned with a column of injection holes, Figure 1a. Further details can be found in [30].

The PIV technique was used in both PPOOLEX [39] and PANDA [40]. In PPOOLEX, a Field-Of-View (FOV) of about 300×300 mm was located at the level of the thermocline (Figure 1a) and image pairs were recorded at a 7 Hz frequency. In PANDA, the FOV was about 900×900 and located in front or above of the injection holes (Figure 4). Each recording sequence consisted in 1024 double images recorded with 5 Hz, covering a recording time of 204.8 s.

2.2. Experimental procedure

In this work a separate effect of the sparger head was systematically investigated by blocking the LRR holes in most of the tests. In total, 9 tests were performed in the PPOOLEX facility in the SPA test series [30], and 4 in the PANDA facility in the HYMERES HP5 series [42]. Within the SPA series, only one exploratory test, the SPA-T7, was run with the LRR holes open and the sparger head blocked.

The steam injection usually started at low momentum (minimum flow rate above chugging domain, see Song et al. [12] and Chan & Lee [15] regime maps for multi-hole and 38 mm single-hole pipes, respectively in Figure 3) to develop stratification in the pool. After reaching a certain temperature difference between the top and bottom of the pool, the mass flow was increased to erode the cold layer.

The focus of the tests was mostly on the oscillatory bubble regime (Figure 3). Only two exploratory tests were performed in the stable cone jet (SPA-T1) and chugging regimes (SPA-T2). The boundary between chugging and oscillatory condensation was observed to be in good agreement with [12] and [15]. The only deviation was observed during the last phase of the SPA-T6 experiment, where, similar to [15], chugging was not observed at high pool temperatures. Note that the difference in injection hole diameter compared to PPOOLEX and PANDA spargers could lead to differences in condensation regimes. However, developing a new condensation regime map is beyond the scope for this work. The fact that single and multi-hole sparger experiments led to similar condensation regimes suggests that the interaction between neighboring jets (for the given pitch to diameter ratio) had a negligible effect on the condensation regimes.

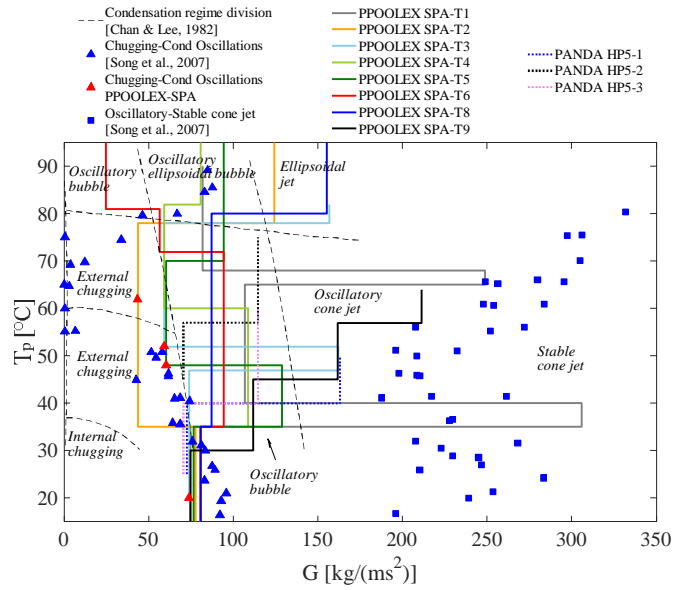


Figure 3: Condensation regime map of the PPOOLEX and PANDA experiments with sparger, using Chan & Lee [15] and Song et al. [12] data. G is the steam mass flux at the injection holes, and T_p the pool bulk temperature. Shakedown tests SPA-T0 and HP5-0, and Helium injection test HP5-5 not included in the map.

3. ANALYSIS OF THE EXPERIMENTAL DATA

3.1. Pool phenomena

Snapshots of the pool temperature and velocity fields during the PANDA HP5-2 experiment are presented in Figure 4. In the low steam injection phase buoyancy drives the water flow upwards to form a hot layer. The interface between the cold and hot layers is found below the sparger. The colder region right below the sparger suggests that jet entrainment sucks water from the cold layer. In the high steam injection phase the larger momentum induced by the steam jets caused a faster erosion of the cold layer. The temperature gradient at the thermocline was as sharp as in the low steam injection phase. This suggests that buoyancy was efficient in suppressing mixing at the thermocline. Thus, modeling of the buoyancy and its effect onto the turbulent diffusion is paramount for simulating the pool behavior.

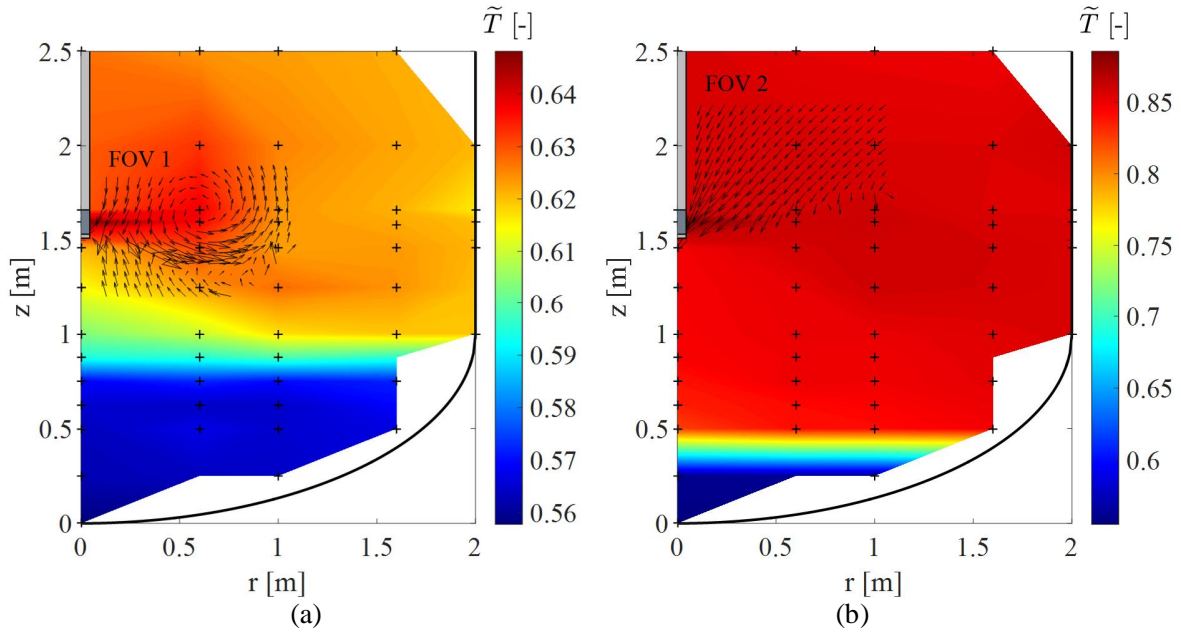


Figure 4: Pool temperature field and velocity vectors during the (a) low and (b) high steam injection phases of the PANDA HP5-2 experiment. Temperature and velocity measurements are time averaged over 200 s. Every 6th velocity vector displayed. Further details of the velocity fields can be observed in Figure 14.

3.1.1. Mixing and erosion of the cold layer

Two regimes of pool temperature homogenization were observed in the tests: mixing and erosion. The transition between these regimes is not sudden, but dependent on the ratio between buoyancy and inertia forces (see Section 3.1.3). In mixing, the momentum is sufficient to overcome buoyancy forces and mix the cold and hot layers. In this process, the temperature of hot layer decreases (2020-1122 mm in Figure 5a) while temperature of the cold layer increases (972-672 mm in Figure 5a). Mixing was observed only in the SPA-T1, where large steam mass fluxes were reached by blocking 3 rings of injection holes. Blowdown pipe experiments performed in the PPOOLEX facility showed a similar mixing regime [23]. Note that a blowdown pipe is more effective for mixing as the injected flow is perpendicular to the cold layer, unlike the radial injection of the sparger head.

In the erosion regime, the injected momentum is not sufficient to cause macroscopic mixing. Only slow erosion of the cold layer at the interface is observed. The interface is sharp, as it can be deduced from the one-at-the-time change in the TCs readings below the thermocline (522-222 mm in Figure 5b), and the absence of noticeable temperature drop in the upper part of the pool.

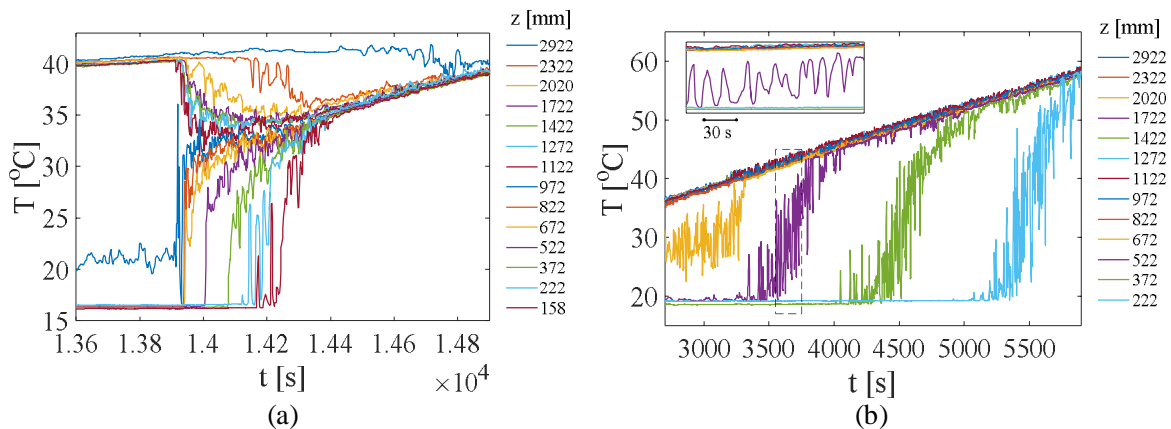
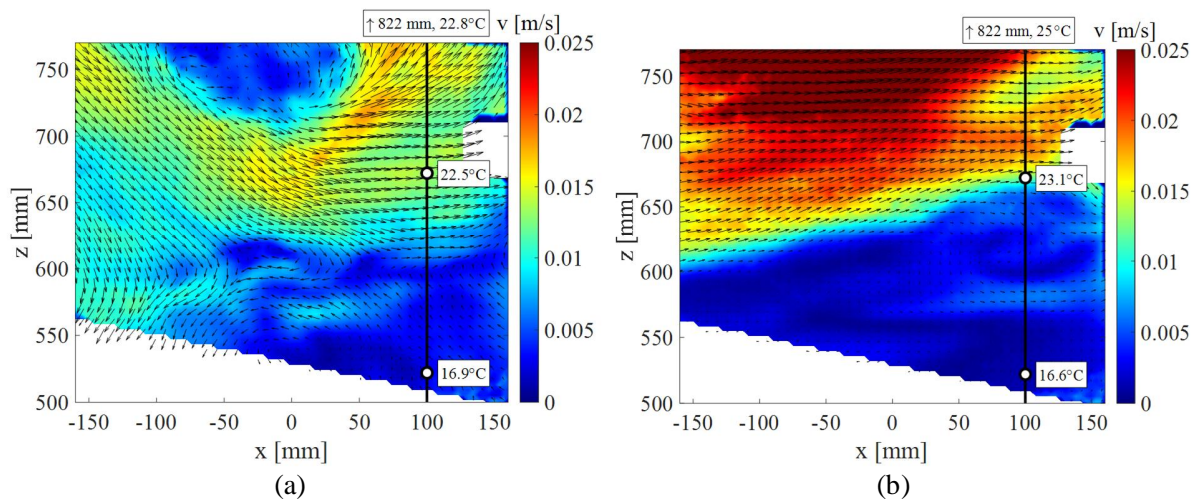


Figure 5: (a) Mixing and (b) erosion of the cold layer during the high steam injection phases of the PPOOLEX SPA-T1 and T4 experiments respectively.

3.1.2. Behavior of the thermocline

PIV data near the thermocline obtained in the PPOOLEX experiments [39] is presented in Figure 6. Based on temperature measurements and data in Figure 6, the thickness of the thermocline can be estimated to be about 50-100 mm. The sudden decrease in the flow velocity indicates the location of the thermocline, which agrees well with the one deduced from the TC measurements. The non-zero mean flow below the thermocline can be induced by tangential shear stress and oscillations of the interface. Large scale turbulent eddies can also be observed. Such eddies can appear intermittently and, as it will be shown in Section 3.1.3, contribute to the slow erosion of the cold layer shown in Figure 5b. Yet, high density gradient act as an effective potential energy barrier which minimizes mixing between the layers.



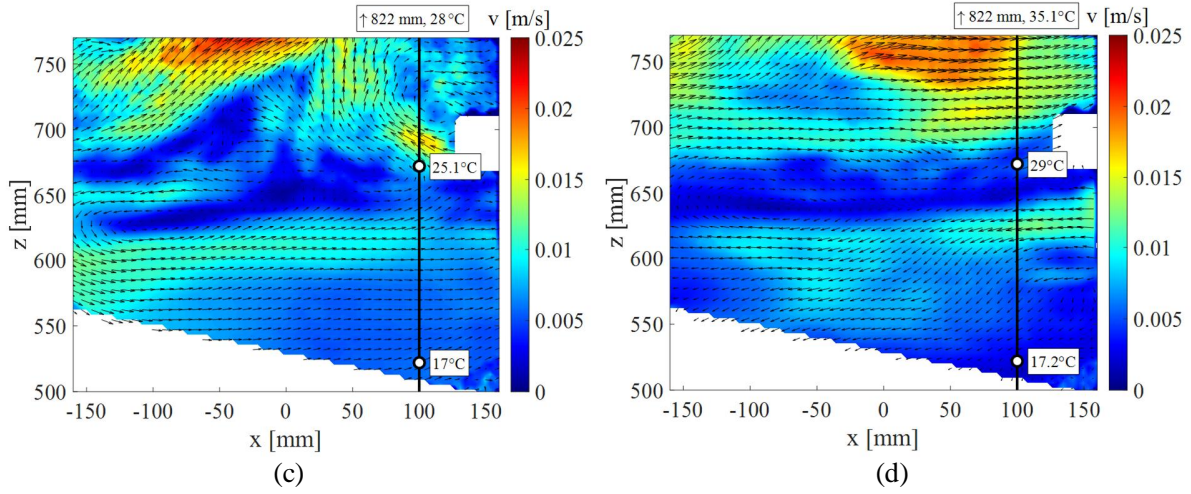


Figure 6: Averaged velocity fields at the thermocline during the first stratification phase of the PPOOLEX SPA T8R experiment. Recording intervals are (a) 1380.1-1383.7 s (b) 1688.6-1695.7 s (c) 2140-2145.7 s (d) 3152.1-3156.4 s. Contour plots generated using three dimensional velocity fields. Vector plots generated using x and z velocities. Every second vector displayed. TC measurements were not located within the PIV plane, but are displayed together for better visualization.

The TCs located at the thermocline showed low frequency and high amplitude temperature oscillations during the erosion phases (Figure 5b). A similar signature can be observed in [19]. A Fast Fourier Transformation (FFT) was applied to the TCs readings after subtracting their time averaged values (0 Hz component). The obtained frequency was much lower than that of typical turbulent fluctuations, suggesting that they are due to large-scale fluid motions.

Work done in [43] shows that the natural oscillation frequencies of a stably stratified two-layer system are dependent on the height and density ratios between the layers. In general, waves at the pool surface are of a higher frequency and shorter wavelength than the ones at the interface between the layers. Assuming a rigid lid at the pool surface, the natural modes of the *interface* oscillations can be computed with equation (2) [43, 44],

$$f_n = \frac{1}{2\pi} \sqrt{gk_n \frac{(\rho_c - \rho_h) \tanh\left(\frac{k_n H_c}{R}\right) \tanh\left(\frac{k_n H_h}{R}\right)}{\rho_c \tanh\left(\frac{k_n H_h}{R}\right) + \rho_h \tanh\left(\frac{k_n H_c}{R}\right)}} \quad (2)$$

where H is the layer height, R the tank radius, and g the gravity. Sub-indexes h and c correspond to the hot and cold layers, and n to the different modes of oscillation, which can be computed using the different roots of the first order Bessel function ($k_1 = 1.84$, $k_2 = 5.33$, $k_3 = 8.54$, etc.).

Comparison between equation (2) and the peaks of the FFT at the pool thermocouples is presented in Figure 7. Despite a noticeable spread of data, the results suggest that the order of magnitude of the frequencies measured by TCs correspond to the predicted first oscillation mode of the of the interface. Other modes could also be super-imposed. However, they could not be measured due to the limited time and space resolution of the TCs. Models which assumed no restrictions on the pool surface motion [43] produced almost identical results.

In a cylindrical tank, the first mode of oscillation corresponds to a standing sinusoidal-type wave with maximum amplitude at two antinodes, located at a half radius, and a node at the pool center and vessel walls [45]. Yet, analysis of the amplitude for all the TCs in the pool showed that there is no clear node (Figure 8). This could be due to the super-position of other modes of oscillation, or to effects induced by density gradients within the hot and cold layers, the mean flow at the upper layer, etc. Moreover, the oscillations seem to have a nearly constant amplitude everywhere, except at vicinity of the vessel walls where it increases.

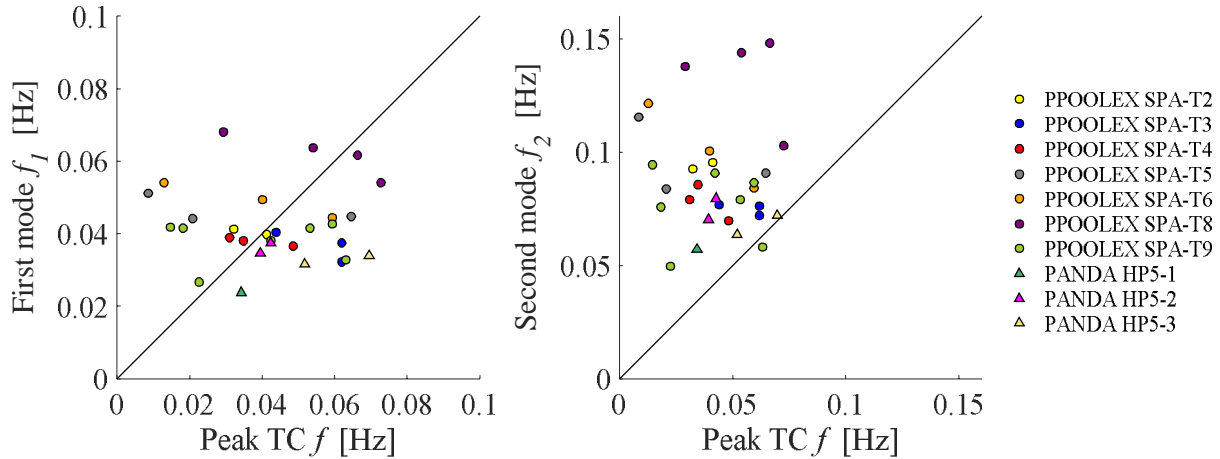


Figure 7: Comparison between the first and second oscillation modes at the thermocline and the peak frequencies measured with the TCs at the thermocline.

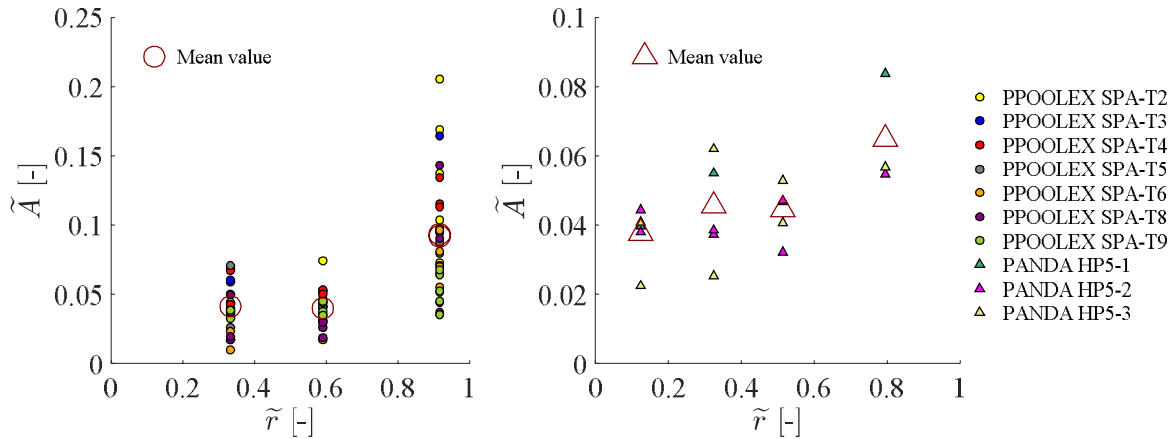


Figure 8: Amplitude of the oscillations of the TCs at the thermocline as a function of the radial distance between the TC and the pool center. The non-dimensional amplitude \tilde{A} corresponds to the amplitude divided by the temperature difference across the thermocline.

3.1.3. Richardson scaling

An important observation from Figure 5b is that it took about 30 min to erode 300 mm of the cold layer. In this section, we analyze the mechanisms which could induce such slow erosion. A review done by Fernando [26] shows that different modes of erosion of a stably stratified layer can be determined by the bulk Richardson number. In a shear and shear free flow, the Richardson number is defined with equations (3) and (4) respectively,

	Richardson number	Erosion velocity	Constants	
Shear	$Ri_s = \frac{\Delta b D}{U^2}$	$\frac{U_E}{U} = C \cdot Ri_s^{-n}$	$C = 0.005 - 5$ $n = 1, 1.5, 2$	(3)
Shear-free	$Ri_{sf} = \frac{\Delta b L_H}{u_H^2}$	$\frac{U_E}{u_H} = C \cdot Ri_{sf}^{-n}$	$C = 1 - 5$ $n = 1, 1.5, 2$	(4)

where Δb is the buoyancy jump across the thermocline, equation (5),

$$\Delta b = g \frac{\rho_c - \rho_h}{\rho_c} \quad (5)$$

D is the mixed layer thickness, U is the velocity above the thermocline (i.e. assuming that the cold layer is stagnant), and L_H and u_H are respectively the length scale of the turbulent eddies and the root-mean-square of the horizontal velocity above the thermocline [46].

The different erosion mechanisms are discussed in [24, 25], where a shear-free turbulent flow was induced by an oscillating grid located at a certain distance above a stable stratified layer. It was observed that at $Ri_{sf} \lesssim 1$ the interface is broken down into fragments which are lifted to mix with the upper part of the pool; at $1 \lesssim Ri_{sf} \lesssim 15$ erosion is caused by the eddies which are able to splash some of the heavy liquid upwards; at $15 \lesssim Ri_{sf} \lesssim 35$ vertical splashing is very sporadic and the erosion is dominated by the shear and collisions of eddies travelling parallel to the interface; at $35 \lesssim Ri_{sf} \lesssim 90$ the erosion is dominated by the intermittent breaking of waves induced by the turbulent eddies, and have a wavelength proportional to the eddy length scale; at $90 \lesssim Ri_{sf}$ sporadic wave breaking is the only erosion mechanism; at Richardson number higher than 100, the erosion velocity is comparable to molecular diffusion.

The vertical erosion velocity U_E of the lower stratified layer can be computed as a function of the Richardson number using equations (3) and (4) [26]. The large spread of constants C and n is attributed to the different erosion mechanisms, secondary flows, and the differences in the experimental setups, such as confinement, turbulent source, mean flow source, etc. Despite these differences, all of them agree on the form of the $C \cdot Ri^{-n}$ equation, known as the ‘‘entrainment law’’.

The steam injection in the PPOOLEX and PANDA experiments is a source of mean flow and turbulence (Figure 14 and Figure 17). When both erosion mechanism are important, the erosion velocity can be expected to be determined by a combination of equations (3) and (4). Unfortunately, estimation of u_H and L_H for the oscillatory bubble regime would require separate effect data, which is beyond the scope of the present work. Thus, we use equation (3), where the buoyancy jump across the thermocline, Δb , was calculated using equation (5) and the mixed layer thickness D was obtained by estimating the vertical distance from the momentum source (sparger injection level in our case) to the thermocline. In previous works, the definition of U varied depending on the momentum source. For example, [47, 48] used two counter-rotating disk pumps which induced an homogeneous parallel flow with velocity U above the lower stratified layer. On the other hand, [49, 50] induced a shear at the pool surface through wind and rotating plates, and defined U as the friction velocity at the pool surface. In this work, we assume that the radial injection of the sparger behaves like a shear source, distributing the momentum along the cross section of the pool. Such friction velocity can be computed with equation (6),

$$U = \sqrt{\frac{\tau}{\rho_L}} = \sqrt{\frac{M_s/A_p}{\rho_L}} = U_s \sqrt{\frac{\rho_s A_i}{\rho_L A_p}} \quad (6)$$

where A_i is the injection hole area and A_p the pool cross section area.

The experimental erosion velocity was calculated using equation (7)

$$U_E = \frac{\Delta z}{\Delta t} \quad (7)$$

where Δz is the vertical distance between two TCs and Δt the time that the thermocline took to pass through these two TCs. The approach used to estimate Δt is presented in Figure 9. First, all of the TCs readings were time-averaged. The time at which the thermocline center passed through the TCs was calculated as the average between the time moments when the temperature was 5 % higher than the cold layer and 5 % lower than the hot layer. Similar results were obtained when taking the average between hot/cold layer temperatures.

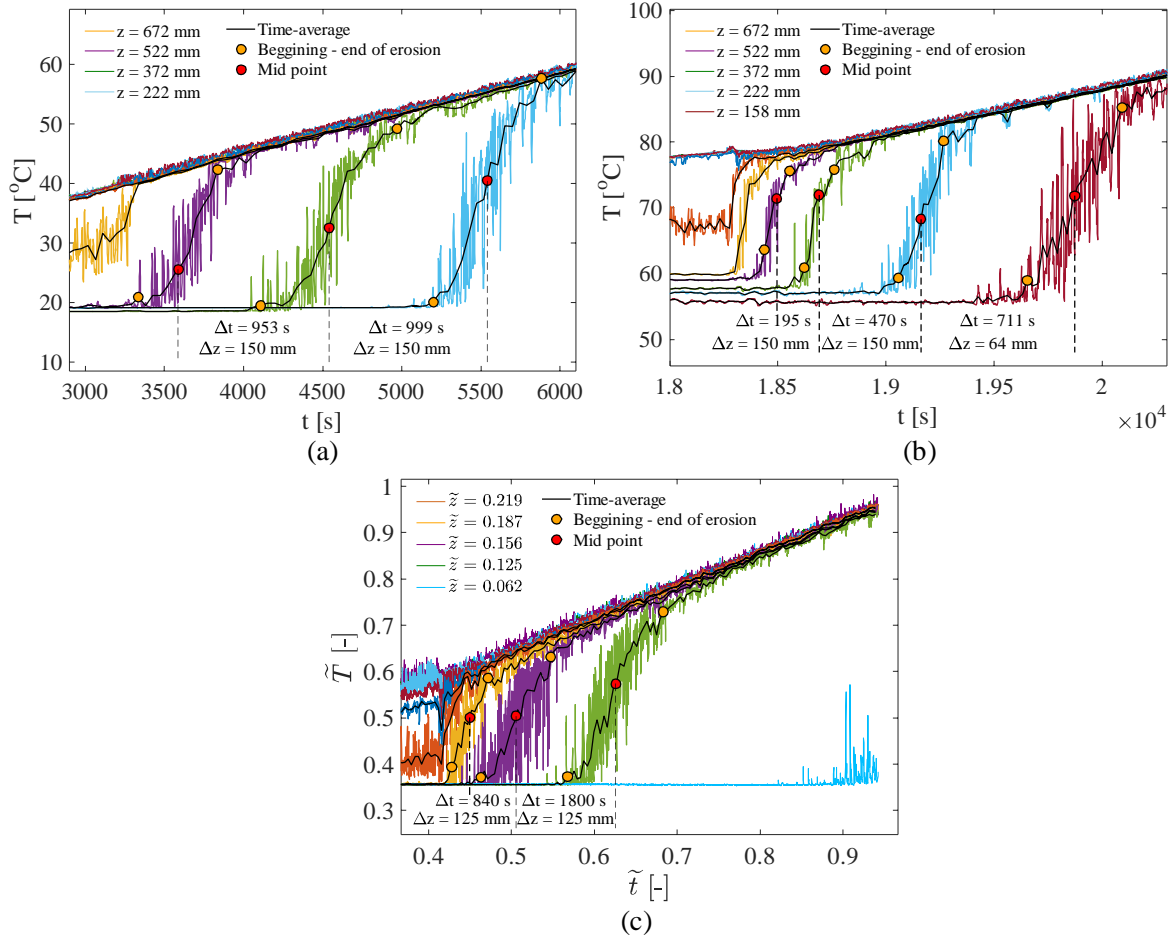


Figure 9: Estimation of the erosion rate of the cold layer for the (a) first erosion phase of the PPOOLEX SPA-T4 experiment (b) last erosion phase of the PPOOLEX SPA_T2 experiment and (c) high steam injection phase of the PANDA HP5-3 experiment.

The results obtained using equations (5), (3), (6) and (7) suggest that the $C \cdot Ri_s^{-n}$ law follows well the erosion velocity of the PPOOLEX and PANDA experiments (Figure 10). Using a non-linear least-square method, the specific constants for our experiments were estimated to be $C = 0.07$ and $n = 1.2$. The same weight was given to all data points. The effect of the temperature difference across the thermocline ΔT can be observed in Points I and II, which had the same steam mass flux and distance to the thermocline. The ΔT of 80 °C in the T8 experiment (Point I) led to a ~20 times slower erosion velocity compared with T3 (Point II), where the ΔT was only 20 °C.

The entrainment law, equation (3), indicates that the velocity should decrease as the erosion progresses due to the gradual increase of the distance D between the sparger and the cold layer. Such reduction was observed in the SPA-T2 and in all the PANDA experiments. However, the SPA-T3 and T4 experiments showed a quasi-constant velocity. The erosion velocities in the SPA-T2 could be affected by the temperature gradients within the cold layer (Figure 12b). The apparent deviation between PPOOLEX and PANDA trends could be caused by differences in the initial momentum source. That is, even if Figure 3 indicates that the regimes should have been similar, the specific geometrical and injection conditions of each experiment could cause the differences. An example of such difference is shown in Section 3.2.2 for the chugging regime.

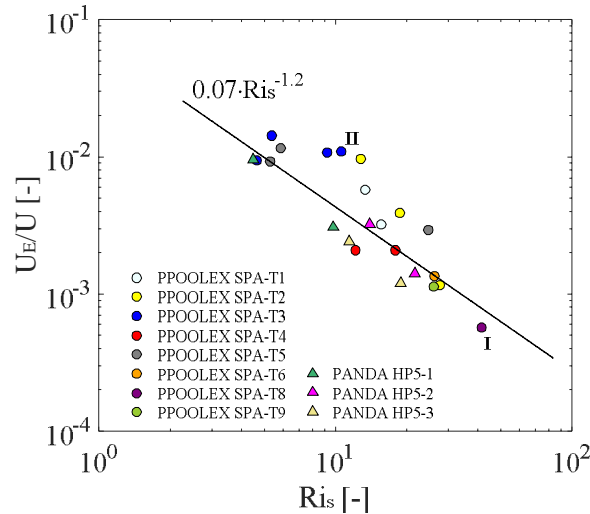


Figure 10: Richardson scaling of the erosion velocity of the cold layer during the PPOOLEX and PANDA experiments with spargers.

The agreement of the PPOOLEX and PANDA experiments with the entrainment law (Figure 10) suggests similar erosion mechanisms as the ones discussed by Fernando et al. [24, 25]. This is also supported by the similarity between the PIV images from Figure 6ac and the images from [25], where we can see the presence of eddies inducing a local de-stabilization of the thermocline. Thus, the slow erosion velocities shown in Figure 5a can be the result of intermittent mixing induced by eddy impingement and breaking of small-scale waves. Since the length-scale of this waves is proportional to the size of the turbulent eddies, we can also conclude that the large-scale low frequency waves detected by the TCs readings (Figure 7) were not the driving erosion mechanism.

Large Eddy Simulations (LES) could be used to resolve the oscillations, but at the expense of very high computational cost, unaffordable for plant safety analysis applications. The Reynolds-Averaged Navier-Stokes (RANS) modeling approach with relatively coarse meshes could give a good prediction for flows with low Ri , whereas its capability to model the wave-breaking mechanism occurring at higher Ri

numbers might be limited. For this case, modelling through an equivalent turbulent viscosity would require a careful selection of the turbulence terms.

3.1.4. Injection of non-condensable gases

Non-condensable gases (e.g. Hydrogen produced during Zirconium cladding oxidation) can be injected into the pool through the spargers connected to the primary system. The PANDA HP5-5 test analyzed the effect of injecting 2 and 4 g/s of Helium combined with 160 g/s of steam. The momentum created by such injection was sufficient to rapidly mix the cold layer with the top layer (Figure 11a). Similar to the observations from [51], video and PIV images from HP5-5 show that Helium moves upwards (Figure 11b) suggesting that a strong natural circulation pattern is created in the pool: axial entrainment in the rising plume, and the downward motion along the vessel walls. Since the downward motion is affected by the vessel diameter, stronger mixing can be expected in case of a pool with a smaller diameter. Therefore, comparison between the small-scale facility from [51], the PANDA facility, and plant scale, should be done with caution.

Helium density is 0.17 kg/m^3 at normal conditions, leading to volumetric flow rates of 0.012 and $0.023 \text{ m}^3/\text{s}$ in the HP5-5 experiment. Hydrogen, whose density is 0.09 kg/m^3 , is expected to be even more efficient for pool mixing at the same mass flow rates due to the larger volumetric flow rates. Small gas bubbles at the same mass flow rate are expected to be more efficient in pool mixing than larger ones due to their larger water-to-gas contact area [52].

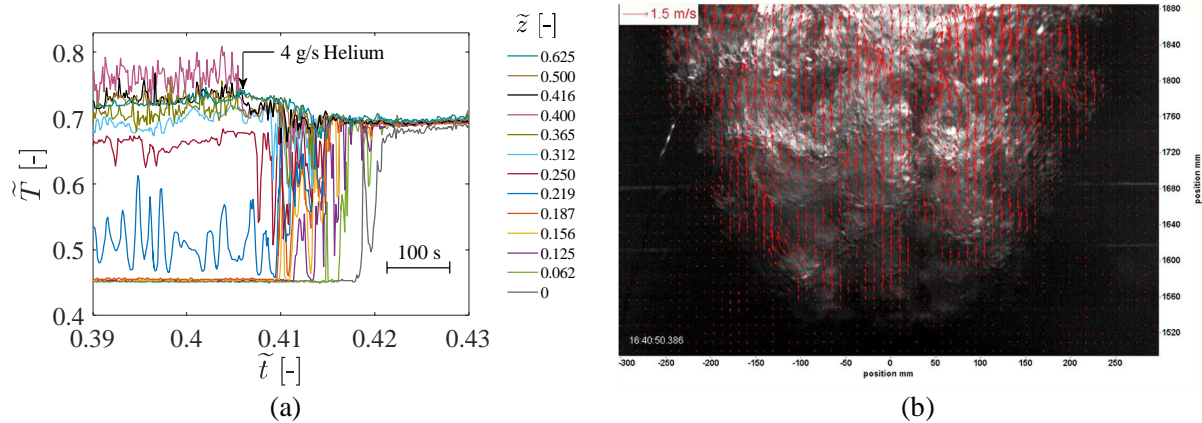


Figure 11: Mixing phase of the PANDA HP5-5 experiment. (a) Temperature evolution along a vertical line of TCs and (b) superposition of PIV and video images during the 4 g/s Helium injection.

3.2. Steam condensation phenomena

3.2.1. Jets at the sparger outlet

In this section, we analyze the temperature and velocity fields induced by the condensing steam jets. The oscillatory bubble regime is characterized by a cyclic growth, detachment, and collapse of steam bubbles of a size similar to the injection hole diameter [53]. The frequency of this cycle can be estimated using Fukuda's correlation ($f = 0.06\Delta T/d$) [54], which gives values between 220 and 850 Hz for the analyzed sparger experiments. Since this frequency is far above the acquisition frequency of all measurements, we will only focus on time-averaged quantiles.

Experimental work done in [11] shows that stable sonic jets condense within 2 to 11 injection hole diameters. Based on the TC mesh data from PPOOLEX, complete condensation in the oscillatory bubble regime occurred within 50 mm, which is about 6 hole diameters (Figure 12). The dependency of the condensation length with the steam mass flux and pool temperature could not be resolved with the 50 mm separation between TCs. Video images from PANDA enabled a qualitative confirmation that the steam jets condensed over a similar distance.

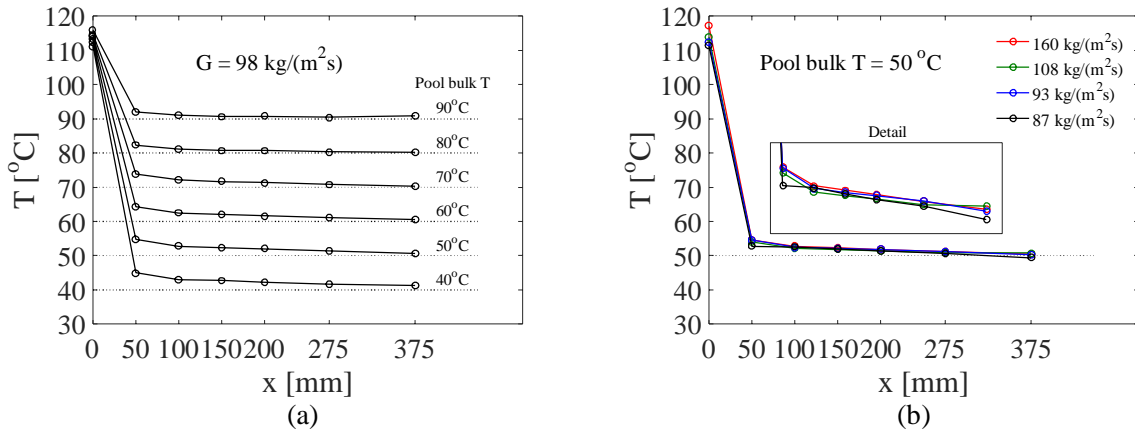


Figure 12: TC measurements in front of the injection holes as a function of the (a) pool bulk temperature, and (b) steam mass flux through the injection holes. Data from PPOOLEX SPA-T3, T4, T5, T6, and T8 experiments. Data point at $x = 0$ mm corresponds to the TC measurements inside the sparger. TC data was time averaged over 200 s.

Parallel water jets induced by the steam injection were observed to merge after a short distance (Figure 13). This is a common effect in parallel jets, caused by the suction effect of the entrainment. According to Ko et al. [55], the distance to complete merging can be estimated as 3 times the pitch plus diameter, which corresponds to 130 and 160 mm for the PPOOLEX and PANDA spargers. This estimate agrees well with the temperature and PIV data in Figure 13.

A downwards inclination of the water jets was observed by the TC mesh in PPOOLEX, Figure 13a, and the PIV system in PANDA, Figure 13b. The inclination was attributed to the downwards component of the steam velocity at the sparger hole outlet. This component is not negligible since the area ratio between injection hole to pipe cross section is about 0.41 and the wall thickness is only 4 mm, not big enough to re-direct the flow to a complete horizontal direction. The injection angle was quantified to be about 10° in a separate PANDA experiment with a gas injection into a gas space (Figure 13b). At low mass flow rates, partial steam condensation inside the sparger and uneven distributions of the steam through the injection holes might affect the angle. A means for measurement of the angle would be necessary in the future experiments. It is recommended to perform sensitivity studies to this parameter during the process of model development and code validation.

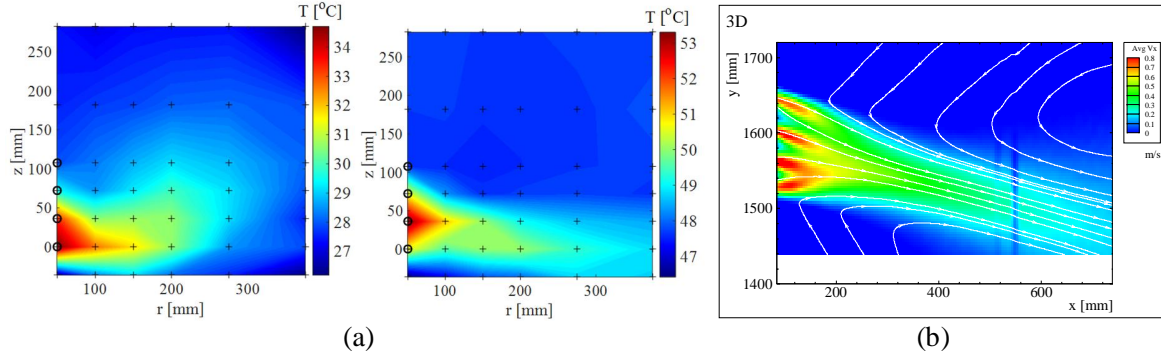


Figure 13: (a) Temperature contours during the first low and high steam injection phase of the PPOOLEX SPA-T3 experiment. TC data was time averaged over 200 s. Symbol (+) corresponds to the TC locations and (\oplus) to first TCs in line with the injection holes. (b) Velocity contours and streamlines during the PANDA gas-to-gas experiment. Velocity data was time-averaged over 200 s.

The flow distribution between different rings of injection holes was estimated using the data from Table 3 together with equations (16) and (17) and a discharge coefficient of $C_D = 0.6$ (Figure 22). It was observed that for PPOOLEX and PANDA the differences in mass flow between the upper and lower rings are expected to be below 2%. Assuming an even flow distribution through each hole, a theoretical injection angle α_{th} was obtained as a vector average of the velocities at each ring:

$$\alpha_{th} = \tan^{-1} \left(\frac{A_i}{2A_{sp}} \left(1 + \frac{1}{N_r} \right) \right) \quad (8)$$

where N_r is the number of rings of holes, A_{sp} the sparger cross section area, and A_i the injection hole area.

Based on equation (8) an angle of $\sim 15^\circ$ was obtained for both PANDA and PPOOLEX (note that they had the same sparger to hole area ratios). The deviation compared to the experimental value of 10° is probably due to secondary flows inside the sparger and buoyancy of the plume. For example, the zero axial velocity at the bottom of the sparger pipe can result in the flow structure that provides an upwards angle at the last ring of holes (Figure 13b). To account for these effects, a C_α coefficient can be used to modify the theoretical estimate, equation (9).

$$\alpha = C_\alpha \alpha_{th} \quad (9)$$

The current experimental results suggest $C_\alpha = 0.67$. Further calibration of C_α should be done using other sparger designs.

In single-phase flows, jets develop a self-similar velocity profile in non-dimensional coordinates. Work done by Choo et al. [56] demonstrated that jets induced by a single-hole steam injection also produce self-similar velocity profiles. The multi-hole injection in PANDA HP5-2 also resulted in a self-similar profile according to the PIV data. In Figure 14 U_0 is the jet centerline velocity, and $r_{1/2}$ the half width radius i.e. $U(r_{1/2}) = U_0/2$. Due to the upwards deflection of the jet induced by buoyancy, $r_{1/2}$ was different in the regions above and below the centerline. The upper/lower estimation of $r_{1/2}$ provides a good self-similarity in respective regions.

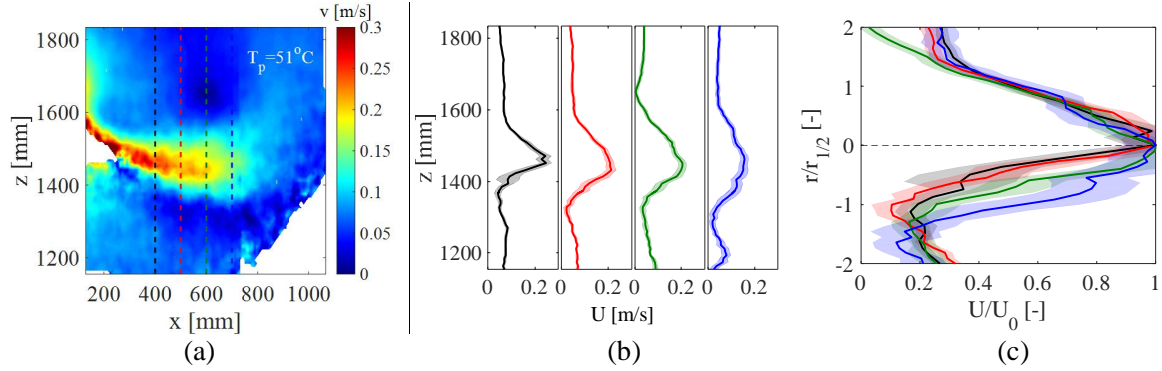


Figure 14: PIV data from the low steam injection phase of the PANDA HP5-2 experiment. (a) Velocity contours, (b) velocity profiles 400, 500, 600, and 700 mm far from the sparger and (c) non-dimensional velocity profiles. Velocity data was time-averaged over 200 s. Shaded areas represent the error of the measurement.

Potential non-uniformities of the azimuthal velocity, which was not measured with PIV, were estimated using standard jet expansion equations. Although the actual flow field should be between round and plane jet, we assumed round jet behavior [57], described by equations (10) and (11),

$$U_0(x) = \frac{BdU_{Li}}{x} \approx \frac{0.10}{x} \quad (10)$$

$$U(x, r) = U_0(x) \exp\left(-K \frac{r^2}{x^2}\right) \quad (11)$$

where U_{Li} and d , the liquid velocity effective diameter of a multi-hole injection, are unknown parameters. The data from Figure 14 can be used to estimate that the nominator in equation (10) is about 0.1. In single-phase flows, the K coefficients for round and plane jets are 77 and 50 respectively [57, 58]. According to Choo et al. [56], a single round condensing steam jet results in similar values of K coefficients varying between 72 to 85. A good agreement with the PIV data from PANDA tests is found when decreasing K to ~ 40 or less (Figure 15). The deviation with the K values from Choo et al. [56] could be due to the effect of multi-hole injection and condensation regimes. Note that all the experiments performed in [56] were in stable condensation regimes appearing above 300 kg/(m²s). The oscillatory bubble regime analyzed in this work might have increased the turbulent diffusion and jet spread. Due to the uncertainty in K , sensitivity studies are recommended in CFD.

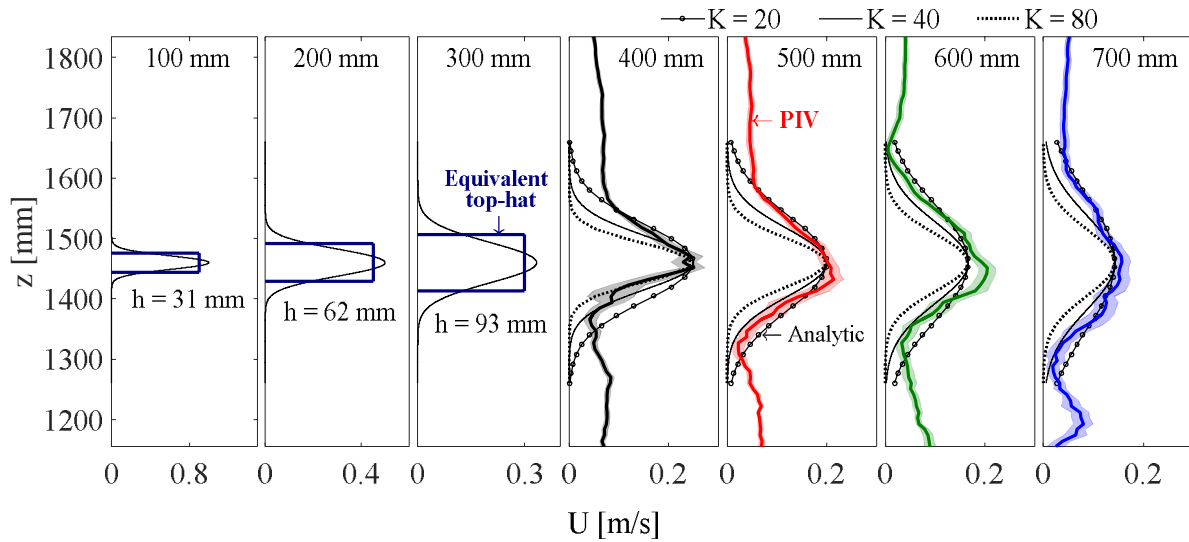


Figure 15: Comparison between the vertical velocity profiles measured with PIV and the analytical profiles obtained with equations (10) and (11) using $K = 20, 40,$ and 80 . Between 100 and 300 mm the analytical curves correspond to $K = 40$ and h to the height of the equivalent top-hat jet. Shaded areas represent the error of the measurement.

Self-similarity of the jets enables modelling of the multi-hole steam injection through a column of holes using a single velocity profile near the sparger, which can be approximated to a top-hat distribution as shown in Figure 15, which provides the same momentum.

The velocity distribution in the azimuthal direction was estimated using equations (10) and (11) and a $K = 40$ and 20 (Figure 16). Note that the number of holes per ring, which can be between 12-24 in the plant, was not preserved in the tests due to the restrictions of the pipe diameter and total injection hole area. A larger number of holes enhances the interaction due to the reduction of the angle between their axial directions, leading to a more homogeneous velocity distribution.

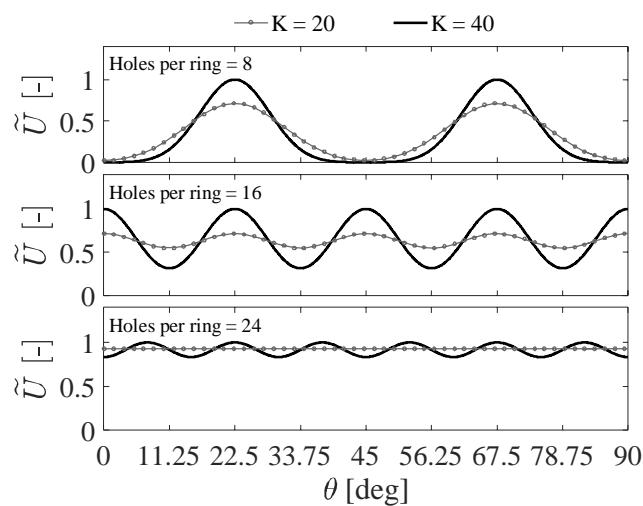


Figure 16: Estimated interaction between neighboring jets in the azimuthal direction for a sparger with 8, 16, and 24 holes, calculated with equations (10) and (11) using $K = 20$ and 40 . The results are applicable for any given distance with a non-dimensional velocity scaled to unity.

The turbulent stresses $\overline{u'_i u'_i}$ induced by the steam injection were calculated from the PIV data using equations (12) and (13),

$$\overline{U}_i = \frac{1}{N_{eff}} \sum_{n=1}^{N_{eff}} U_{i_n} \quad (12)$$

$$\overline{u'_i u'_i} = \frac{1}{N_{eff}} \sum_{n=1}^{N_{eff}} (U_{i_n} - \overline{U}_i)^2 \quad (13)$$

where U is the instantaneous flow velocity, \overline{U} its time-averaged value, sub-index i the axial x and vertical z directions, and N_{eff} the number of valid samples within a 200 s time frame considering statistical independence [41]. The turbulent kinetic energy was calculated with equation (14),

$$k = \frac{1}{2} (\overline{u'_x u'_x} + 2\overline{u'_z u'_z}) \quad (14)$$

where the y velocity component not measured with the 2D PIV system was assumed to be equal to the z component (axis-symmetry around the x axis). The turbulent intensity was calculated with equation (15),

$$I_i = \sqrt{\frac{\overline{u'_i u'_i}}{U_0^2}} \quad (15)$$

where U_0 is the jet centerline velocity. Using equations (12), (13) and (15), the turbulent intensity was observed to vary between 50 to 90 % (Figure 17b). Similar extremely high values were observed in other PIV recordings obtained in the PANDA experiments. In the work done by Van Wissen et al. [59] the maximum measured turbulent intensities generated by a single-hole steam injection into a pool were about 30 %. Thus, further measurements using other techniques might be needed to confirm these results.

A source of uncertainty not reflected in the shaded areas from Figure 17 is the change in the refractive indices. These changes can be induced by temperature gradients along the path of each beam of light travelling from the tracer to the camera. Assuming that this change has no directional bias, time-averaged values such as mean velocities would minimize this error in a large enough time window. However, variables computed as an absolute value (such as the turbulent stresses, equation (13)) will lead to an artificial increase of the calculated quantity. Note that a ~25 % turbulence intensity was measured at $z = 1800$ mm, which could be an indicator for the magnitude of turbulence intensity over-estimation.

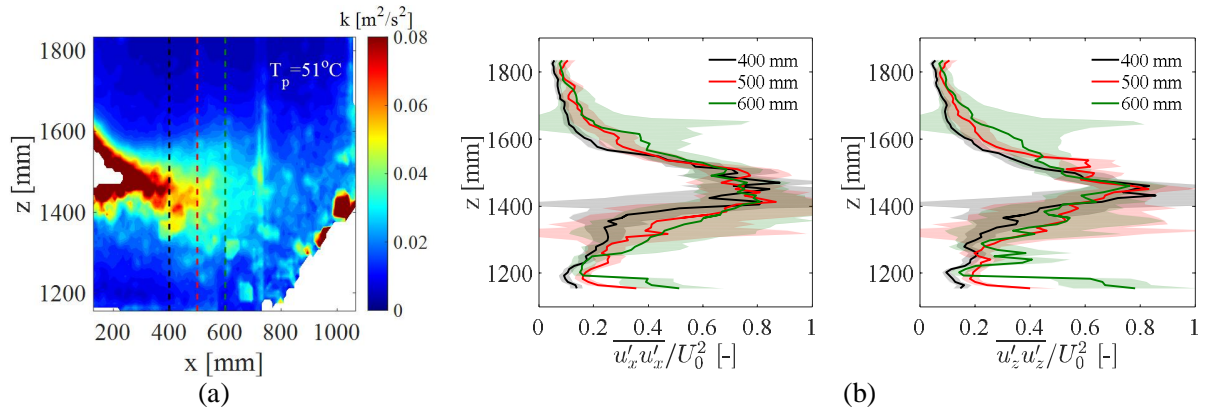


Figure 17: PIV data from the low steam injection phase of the PANDA HP5-2 experiment. (a) Turbulent kinetic energy contours and (b) square of the turbulent intensities in the axial and vertical directions. Velocity data was time-averaged over 200 s. Shaded areas represent the error of the measurement.

The PIV data obtained in PANDA was also used to estimate the ratio of turbulent to molecular viscosity. Ratios of up to $1e6$ were obtained at the jet centerline and $\sim 4e4$ in the $z = 1800$ mm region. These large values can be affected by the accumulation of refractive indices errors when computing derivatives of the instantaneous velocities (needed to calculate the turbulent dissipation ε). Other experimental techniques should be developed in further experiments to measure this quantity.

3.2.2. Chugging regime

In the PPOOLEX SPA-T2 experiment, chugging was observed in the video images and in the large-amplitude temperature oscillations of the TCs inside the sparger pipe, Figure 18. At low pool temperatures, the momentum induced by the chugging was enough to erode the cold layer and maintain the pool well mixed. Increasing pool temperatures reduced the chugging momentum, leading to the pool re-stratification at $T_p \approx 60$ °C. At 65 °C chugging was completely suppressed and the pool was re-stratified.

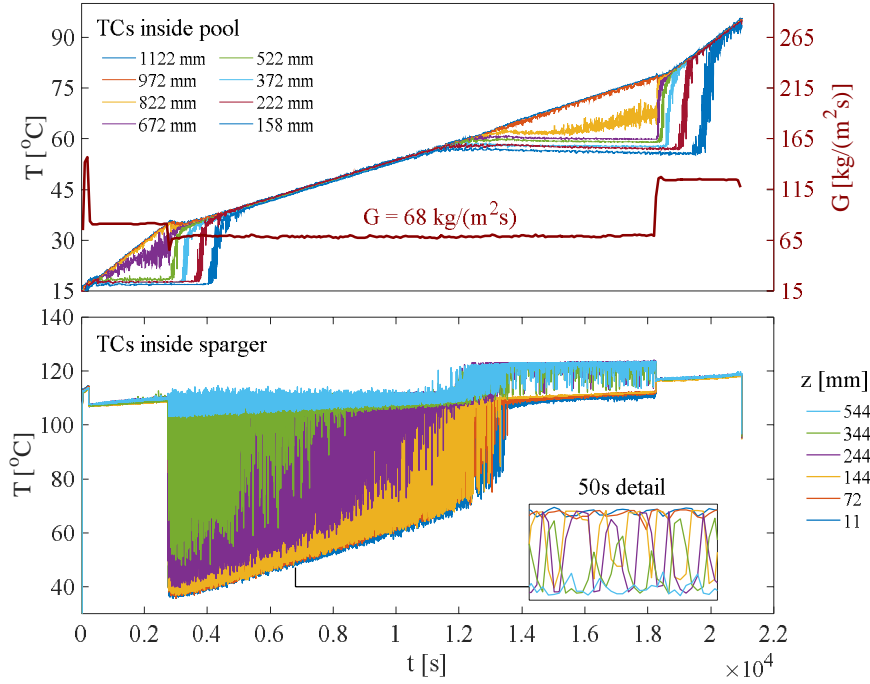


Figure 18: Steam chugging during the PPOOLEX SPA-T2 experiment. Elevation 0 mm of the TCs inside the pool corresponds to the pool bottom, and in the TCs inside the sparger, to the sparger bottom.

The frequency of the liquid level oscillations inside the sparger were estimated using the 20 Hz TC mesh measurements. A FFT was applied to 500 s intervals to capture the effect of the pool temperature. As we can see in Figure 19b, the frequency was maintained constant at about 1.8 Hz, and suddenly dropped to zero values at $T_p \approx 65^\circ\text{C}$. The amplitude of the oscillations was estimated using the TCs inside the sparger pipe. Contrary to the PPOOLEX MIX experiments [23], the 100 mm distance between TCs was not enough to get an accurate estimation of the amplitude. Thus, the results in Figure 19a are given with the error corresponding to the distance between TCs.

Based on the frequency and amplitude, the effective velocity induced by the chugging in the liquid can be computed as $U_{eff} = \sqrt{2}fA$, and the effective momentum as $M_{eff} = \rho_L A_i U_{eff}^2$ [6]. Figure 19c shows that the momentum is indeed reduced substantially at $T_p \approx 65^\circ\text{C}$, explaining the re-stratification of the pool.

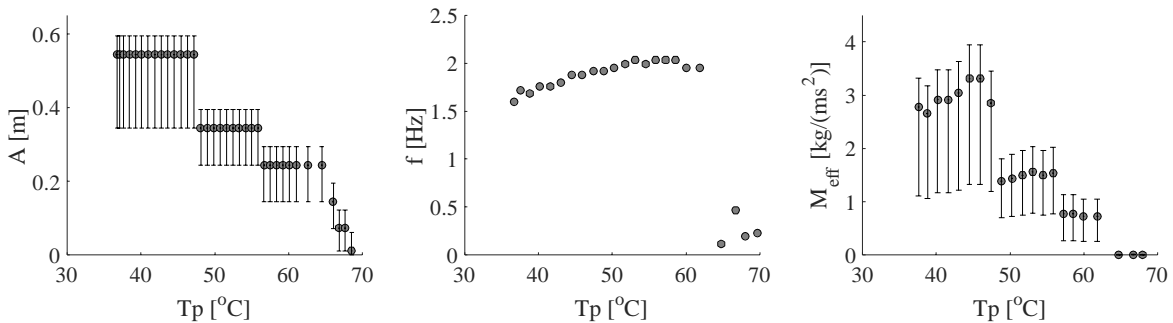


Figure 19: (a) Amplitude and (b) frequency of the liquid level oscillations inside the sparger as a function of the pool temperature, and (c) effective momentum induced into the pool.

Unstable condensation and temperature oscillations were also observed in the video recordings and TCs measurements inside the sparger of the PANDA shakedown test, which was run at similar conditions as the PPOOLEX SPA-T2. However, these oscillations were of much lower amplitude compared to PPOOLEX and were not sufficient to mix the pool (Figure 20). Moreover, the video images recorded in PANDA did not show the regular steam jet pulses which could be observed in the PPOOLEX videos and TC mesh. Given the differences between PPOOLEX and PANDA, it can be concluded that the chugging boundary in terms of steam mass flux and pool temperature can be different for different sparger designs (such as T-quenchers).

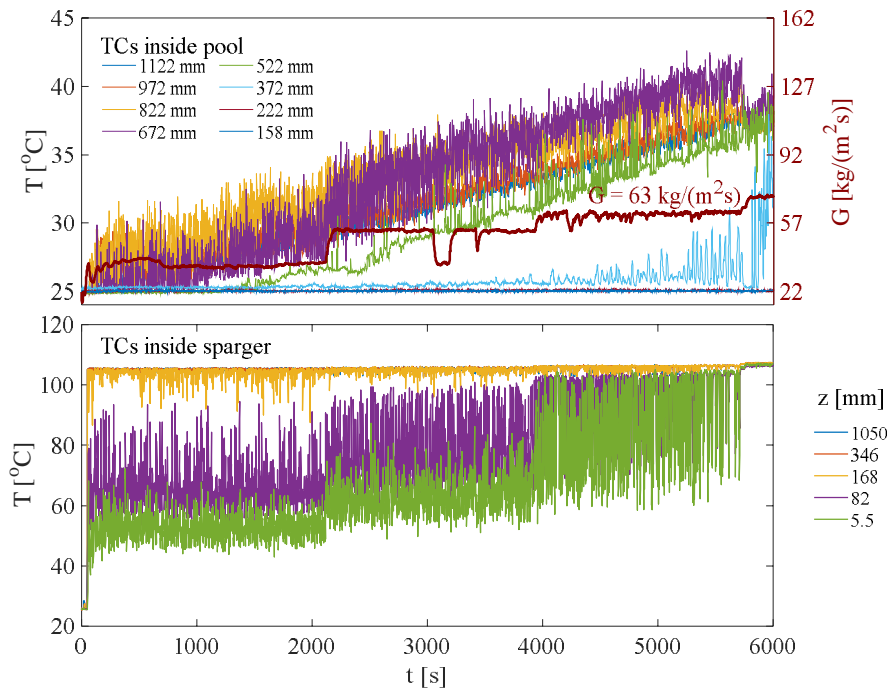


Figure 20: Temperature oscillations inside the sparger during the PANDA HP5-0 test. Elevation 0 mm of the TCs inside the pool corresponds to the pool bottom, and in the TCs inside the sparger, to the sparger bottom.

3.2.3. Discharge coefficient

In this section, we calculate the discharge coefficient C_D at the sparger injection holes, equation (16),

$$C_D = \frac{\dot{m}_{exp}}{\dot{m}_{th}} \quad (16)$$

where \dot{m}_{exp} and \dot{m}_{th} are the experimental and theoretical mass flow rates, respectively. According to [60], the main variable determining the losses is the ratio between the total injection hole area and the pipe cross section area. PPOOLEX and PANDA spargers were designed with the same ratio $\beta = 0.41$ at the sparger head. Therefore, similar losses can be expected in both designs.

The theoretical mass flow rate was calculated assuming a steady-state, isotropic compressible flow, equation (17)

$$\dot{m}_{th} = A_i \sqrt{\rho_1 P_1 \frac{2\gamma}{(\gamma-1)} \left(\left(\frac{P_2}{P_1} \right)^{2/\gamma} - \left(\frac{P_2}{P_1} \right)^{(\gamma+1)/\gamma} \right)} \quad (17)$$

where sub-index 1 and 2 indicate up- and downstream conditions respectively.

The assumptions used to derive equation (17) limit its applicability to the steady adiabatic flows. Loss of accuracy can be expected in case with significant flow pulsations and steam condensation inside the sparger pipe. For example, in the PPOOLEX SPA-T1, T7, and T9 experiments, which were run with only 1 ring of holes. This means that for the same steam mass flux at the injection holes the mass flow inside the sparger pipe was 4 times lower than in other test, increasing the possibility of condensation.

P_1 in equation (17) was obtained assuming saturated steam conditions inside the sparger. Since all the experiments were run at sub-sonic conditions (average Mach 0.27, maximum 0.9 in SPA-T1), the pressure at the injection holes outlet P_2 was assumed to be equal to the hydro-static pressure of the pool P_∞ at the same level.

The estimated discharge coefficients for all the PPOOLEX and PANDA tests are presented in Figure 21. The data from both facilities overlap, ranging between 0.5 to 0.8. Apparently, steam condensation inside the sparger could lead to negative energy losses ($C_D > 1$) in the estimations for SPA-T1 and T7 experiments, and in the very low steam mass flux conditions of the SPA-T4. Above 120 kg/(m²s) the discharge coefficient seems to increase asymptotically with the steam mass flux. The dependency of C_D on the pool temperature (Figure 21b) showed that the lowest values are reached at about 60 °C. According to [61] the amplitude of the pressure pulses induced by a multi-hole steam injection in the oscillatory bubble regime reach their maximum at a $\Delta T/T_s$ between 0.2 to 0.45, which corresponds to pool temperatures of about 60 to 80 °C. Below and above these temperatures, the amplitude tends to be zero. Therefore, it is possible that higher pressures inside the sparger would be needed to inject steam at the conditions between 60 to 80 °C, leading to lower values of C_D .

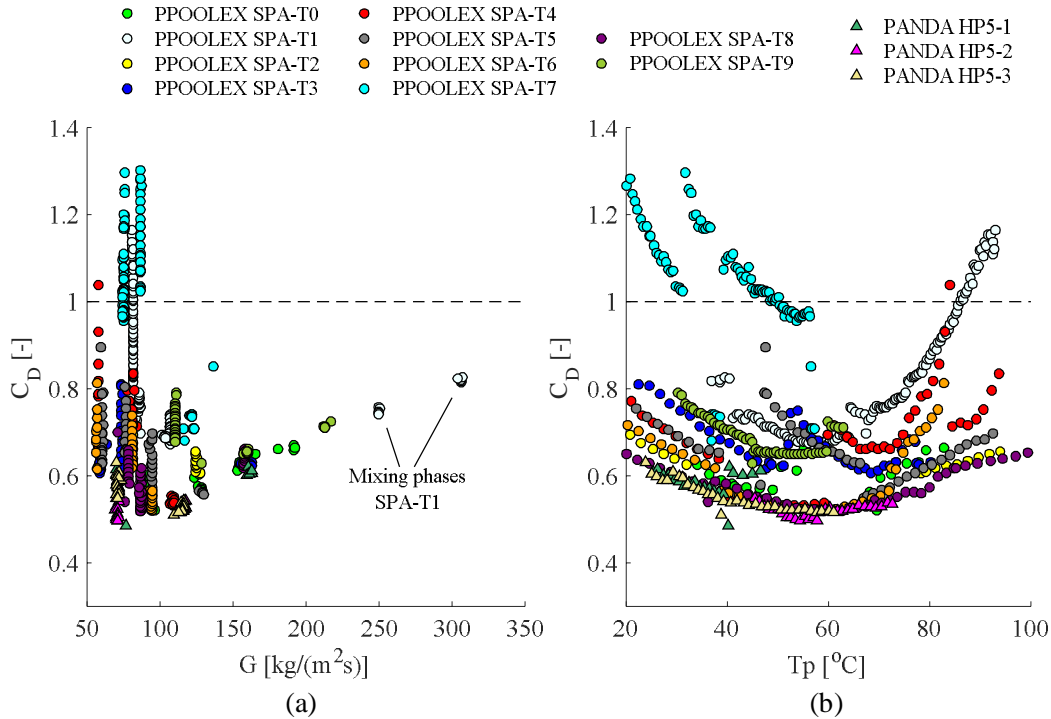


Figure 21: Discharge coefficient as a function of the (a) pool temperature and (b) steam mas flux at the injection holes.

The work done by Kayser & Shambaugh [62] concluded that the discharge coefficient for a compressible flow is well correlated with the dimensionless pressure ratio $\widetilde{\Delta P}$ given by equation (18).

$$\widetilde{\Delta P} = \frac{P_1 - P_2}{P_{crit} - P_2} \quad (18)$$

Using this ratio, Figure 22 presents the same data set as in Figure 21, but displaying only the loss coefficients when the steam mass flux inside the sparger pipe was higher than 25 kg/(m²s). We can see in Figure 22 that experimental data points are well grouped, and close to the $\widetilde{\Delta P}$ correlation proposed in [62].

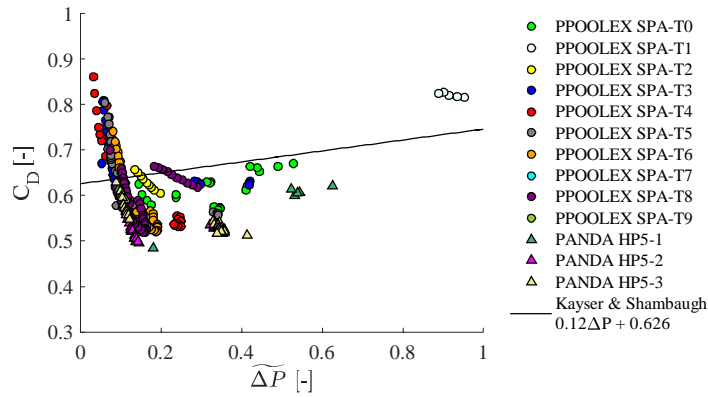


Figure 22: Discharge coefficient as a function of the dimensionless pressure ratio. Comparison with the correlation proposed by Kayser & Shambaugh [62].

4. CONCLUSIONS

The interpretation of the pool experiments with vertical spargers performed in the PPOOLEX and PANDA facilities is discussed in detail in this work. The focus was on the sub-sonic oscillatory bubble regime, expected in a long-term steam injection during SBO-type scenarios. Despite the differences in scales, similar pool and steam condensation behavior were observed in PPOOLEX and PANDA. The major findings and implications for modeling approaches are summarized below:

1. A thin thermocline layer (interface between hot-cold layers) of about 50 mm was maintained in the pool during the stratification and slow erosion phases. In CFD models, fine grid resolution would be required in the vertical direction to resolve such a layer.
2. Low frequency waves (< 1 Hz) are observed at the thermocline during the erosion phase. These waves correspond to the first natural mode of oscillations of the stratified layers and might have little effect on the erosion, and thus of low interest in the modeling of the erosion rate.
3. The slow erosion of the cold layer is expected to be dominated by intermittent eddy impingement and breakup of smaller wavelength interfacial waves at the thermocline. Adequate modelling of these phenomena in RANS will require a careful selection of the turbulence generation and

dissipation terms. Using LES to resolve the individual eddies would lead to a very high computational cost.

4. Based on the experimental data, a Richardson correlation was proposed to predict the vertical erosion velocity of the cold layer as a function of the steam injection conditions and pool dimensions. This could be used in lumped parameter codes where the flow structure and wave breaking erosion phenomena cannot be resolved.
5. Helium injection induced a strong natural circulation pattern that was able to mix the pool. Hydrogen is expected to be even more efficient in the mixing due to its lower density. The effect of the gas flow rate on the mixing time scale has not been investigated.
6. The steam jets condense within ~6 injection hole diameters. This would be the minimum distance where single-phase liquid boundary conditions can be applied in a CFD simulation.
7. The steam jets have a downwards inclination of about 10° at the sparger outlet due to the downwards velocity component at the hole orifice. Since this angle would increase the momentum directed towards the cold layer, it should be considered in CFD modeling.
8. The jets near the sparger outlet merge in the vertical direction. Apparently, a self-similar jet is formed as a result. No measurements are available to assess if merging in the azimuthal direction occurs. An analytical assessments suggest that such merging might not occur in experiments at certain conditions; however, it is more likely to occur in plant conditions where azimuthal angles between neighboring holes are smaller. Thus, modelling of each individual column of jets might be needed in a CFD analysis of the tests.
9. Extremely high turbulence intensity of 50 to 90 %, were measured by the PIV system. Further experimental work is necessary to confirm this finding. Possibility of higher levels of turbulence have to be taken into account in the boundary conditions for the CFD models.
10. Chugging regime was observed at low steam mass fluxes, with a frequency of about 1.8 Hz and an amplitude between 544 and 0 mm. Chugging was completely suppressed at pool temperatures higher than $\sim 65^\circ\text{C}$. The frequency and amplitude of the chugging oscillations were used to estimate the effective momentum, which can be used as a boundary condition in a CFD simulation, instead of simulating the direct steam condensation phenomena.
11. The ratio between the sparger pipe cross section area and injection hole area determines the loss coefficient through the injection holes, which was observed between 0.5 and 0.8. This could be used to estimate the upstream pressure needed to inject steam into the pool.

Further experiments on steam injection through sparger are necessary in order to get a better understanding of the wave-breaking mechanisms responsible for the erosion of the cold layer. Measurements of the turbulent intensity should also be further performed to confirm the large range obtained in the PANDA experiments. Once the phenomena are well understood, the effect of a steam injection through the LRR and sparger head should also be addressed. Further data on chugging regime would also be needed to generate maps of frequency and amplitude which can be used to predict the effective momentum.

ACKNOWLEDGMENTS

This work was funded by Swedish Radiation Safety Authority (Strålsäkerhetsmyndigheten) the NORTHNET-RM3, the Nordic Nuclear Safety Research (NKS), and the countries participating in the OECD/NEA HYMERES project. The authors would like to thank all the members of the Management

Board and the Programme Review Group of the HYMERES project for the discussions of the test programme and results.

REFERENCES

1. Pershagen, B., 1994. Light Water Reactor Safety. Pergamon Press, section 8.1.
2. Mizokami, S., Yamanaka, Y., Watanabe, M., Honda, T., 2013. State of the art MAAP analysis and future improvements on TEPCO Fukushima-Daiichi NPP accident. Proceedings of 15th international conference on Nuclear Reactor Thermal-Hydraulics (NURETH-15), Pisa, Italy, paper 536.
3. Mizokami, S., Yamada, D., Honda, T., Yamauchi, D., Yamanaka, Y., 2016. Unsolved issues related to thermal-hydraulics in the suppression chamber during Fukushima Daiichi accident progressions. *Journal of Nuclear Science and Technology*, 53 (5), 630-638.
4. Pellegrini, M., et al., 2016. Benchmark study of the accident at the Fukushima Daiichi NPS: best-estimate case comparison. *Nuclear Technology*, 196 (2), 198-210.
5. Li, H., Kudinov, P., 2010. Effective Approaches to Simulation of Thermal Stratification and Mixing in a Pressure Suppression Pool. OECD/NEA & IAEA Workshop CFD4NRS-3, Bethesda, MD, USA, September 14-16, 2010.
6. Li, H., Villanueva, W., Kudinov, P., 2014. Approach and Development of Effective Models for Simulation of Thermal Stratification and Mixing Induced by Steam Injection into a Large Pool of Water. *Science and Technology of Nuclear Installations*, 2014, Article ID 108782.
7. Li, H., Villanueva, W., Puustinen, M., Laine, J., Kudinov, P., 2014. Validation of Effective Models for Simulation of Thermal Stratification and Mixing Induced by Steam Injection into a Large Pool of Water. *Science and Technology of Nuclear Installations*, 2014, Article ID 752597.
8. Villanueva, W., Li, H., Puustinen, M., Kudinov, P., 2015. Generalization of experimental data on amplitude and frequency of oscillations induced by steam injection into a subcooled pool. *Nuclear Engineering and Design*, 295, 155-161.
9. Gallego-Marcos, I., Villanueva, W., Kudinov, P., 2018. Modelling of Pool Stratification and Mixing Induced by Steam Injection through Blowdown Pipes. *Annals of Nuclear Energy*, 112, 624-639.
10. Li, H., Villanueva, W., Puustinen, M., Laine, J., Kudinov, P., 2018. Thermal stratification and mixing in a suppression pool induced by direct steam injection. *Annals of Nuclear Energy*, 111, 487-498.
11. Song, C.H., Cho, S., Him, H.Y., Bae, Y.Y., Chung, M.K., 1998. Characterization of direct contact condensation of steam jets discharging into a subcooled water. Proceedings of IAEA Technical Committee Meeting, PSI, Villigen.
12. Song, C.H., Cho, S., Kang, H.S., 2012. Steam jet condensation in a pool: From fundamental understanding to engineering scale analysis. *Journal of Heat Transfer*, 134 (3), 15 pages.
13. Simpson, M.E., Chan, C.K., 1982. Hydrodynamics of a subsonic vapor jet in subcooled liquid. *Journal of Heat Transfer*, 104 (2), 271-278.
14. Wu, X.Z., Yan, J.J., Li, W.J., Pan, D.D., Liu, G.Y., Li, W.J., 2009. Condensation regime diagram for supersonic/sonic steam jet in subcooled water. *Nuclear Engineering and Design*, 239 (12), 3142-3150.
15. Chan, C.K., Lee, C.K.B., 1982. A regime map for direct contact condensation. *International Journal of Multiphase Flow*, 8 (1), 11-20.
16. Aya, I., Nariai, H., 1987. Boundaries between regimes of pressure oscillations induced by steam condensation in pressure suppression containment. *Nuclear Engineering and Design*, 99, 31-40.
17. Solom, M., Kirkland, K.V., 2016. Experimental investigation of BWR Suppression Pool stratification during RCIC system operation. *Nuclear Engineering and Design*, 310, 564-569.
18. Song, D., Erkan, N., Jo, B., Okamoto, K., 2014. Dimensional analysis of thermal stratification in a suppression pool. *International Journal of Multiphase Flow*, 66, 92-100.
19. Zhang, Y., Lu, D., Wang, Z., Fu, X., Cao, Q., Yang, Y., Wu, G., 2016. Experimental research on the thermal stratification criteria and heat transfer model for the multi-holes steam ejection in IRWST of AP1000 plant. *Applied Thermal Engineering*, 107, 1046-1056.
20. Moon, Y.T., Lee, H.D., Park, G.C., 2009. CFD simulation of steam jet-induced thermal mixing in subcooled water pool. *Nuclear Engineering and Design*, 239, 2849-2863.

21. Gamble, R.E., Nguyen, T.T., Shiralkar, B.S., Peterson, P.F., Greif, R., Tabata, H., 2001. Pressure suppression pool mixing in passive advanced BWR plants. *Nuclear Engineering and Design* 204 (1-3), 321-336.
22. Gregu, G., Takahashi, M., Pellegrini, M., Mereu, R., 2017. Experimental study on steam chugging phenomenon in a vertical sparger. *International Journal of Multiphase Flow*, 88, 87-98.
23. Laine, J., Puustinen, M., Räsänen, A., 2013. PPOOLEX experiments on the dynamics of free water surface in the blowdown pipe. *Nordic Nuclear Safety Research*, NKS-281.
24. Fernando, H.J.S., Hunt, J.C.R., 1997. Turbulence, waves and mixing at shear-free density interfaces. Part 1. A theoretical model. *Journal of Fluid Mechanics*, 347, 197-234.
25. McGrath, J.L., Fernando, H.J.S., Hunt, J.C.R., 1997. Turbulence, waves and mixing at shear-free density interfaces. Part 2. Laboratory experiments. *Journal of Fluid Mechanics*, 347, 235-261.
26. Fernando, H.J.S., 1991. Turbulent mixing in stratified fluids. *Annual Review of Fluid Mechanics*, 23, 455-93.
27. Nokes, R.I., 1988. On the entrainment rate across a density interface. *Journal of Fluid Mechanics*, 188, 185-204.
28. Hopfinger, E.J., Toly, J.A., 1976. Spatially decaying turbulence and its relation to mixing across density interfaces. *Journal of Fluid Mechanics*, 78, 155-175.
29. Peterson, P.F., 1994. Scaling and analysis of mixing in large stratified volumes. *International Journal of Heat and Mass Transfer*, 37, 97-106.
30. Laine, J., Puustinen, M., Räsänen, A., 2015. PPOOLEX Experiments with a Sparger. *Nordic Nuclear Safety Research*, NKS-334.
31. Paladino, D., Dreier, J., 2012. PANDA: A Multipurpose Integral Test Facility for LWR Safety Investigation. *Science and Technology of Nuclear Installations*, 2012, Article ID 239319, 9 pages.
32. D'Auria, F., Galassi, G.M., 2010. Scaling of nuclear reactor system thermal-hydraulics. *Nuclear Engineering and Design*, 240 (10), 3267-3293.
33. GOTHIC Thermal Hydraulic Analysis Package, Version 8.1(QA). EPRI, Palo Alto, CA: 2014.
34. Su, T.M., 1981. Suppression Pool Temperature Limits for BWR Containments. US-NRC, NUREG-9783.
35. Li, X., Zhang, M., Du, Z., Fu, X., 2014. Scaling analysis of coolant spraying process in automatic depressurized system. *Annals of Nuclear Energy*, 72, 350-357.
36. Sonin, A.A., 1981. Scaling laws for small-scale modeling of steam relief into water pools. *Nuclear Engineering and Design*, 65 (1), 17-21.
37. Nilsson, L., 2007. Development of an Input Model to MELCOR 1.8.5 for Oskarshamn 3 BWR. SKI Research report, ISSN 1104-1374.
38. Lahey, R.T., Moody, F.J., 1993. *The Thermal Hydraulics of a Boiling Water Nuclear Reactor*. 2nd edition, American Nuclear Society, La Grange Park, Ill, USA, page 582.
39. Puustinen, M., Pyy, L., Laine, J., Räsänen, A., 2017. Sparger tests in PPOOLEX on the behaviour of thermocline. *Nordic Nuclear Safety Research*, NKS-382.
40. Kapulla, R., Uong, D., Zimmer, C., Paladino, D., 2017. PIV measurements in the vicinity of a steam sparger in the PANDA facility. *Nuclear Engineering and Design*, article in press.
41. Sciacchitano, A., Wieneke, B., 2016. PIV uncertainty propagation. *Measurement Science and Technology*, 27 (8), 16 pages.
42. Kapulla, R., Mignot, G., Paranjape, P., Paladino, D., Fehlmann, M., Suter, S., 2015. OECD/NEA HYMERES project: HP5 Test Results. 6th Meeting of the Programme Review Group and Management Board of the HYMERES Project, PSI Villigen, Switzerland, 17-19 November.
43. Craig, W., Guyenne, P., Sulem, C., 2011. Coupling between internal and surface waves. *Natural Hazards*, 57 (3), 617-642.
44. Tang, Y., 1993. Dynamic response of tank containing two liquids. *Journal of Engineering Mechanics*, 119 (3), 531-548.
45. Wang, Z., Zou, L., Zong, Z., 2016. Three dimensional sloshing of stratified liquid in a cylindrical tank. *Ocean Engineering*, 119, 58-66.

46. De Silva, I.P.D., Fernando, H.J.S., 1992. Some aspects of mixing in a stratified turbulent patch. *Journal of Fluid Mechanics*, 240, 601-625.
47. Narimousa, S., Long, R.R., Kitaigorodsk, S.A., 1986. Entrainment due to turbulent shear flow at the interface of a stably stratified fluid. *Tellus*, 38A, 76-87.
48. Strang, E.J., Fernando, H.J.S., 2001. Entrainment and mixing in stratified shear flows. *Journal of Fluid Mechanics*, 428, 349-386.
49. Kato, H., Phillips, M., 1969. On the penetration of a turbulent layer into stratified fluid. *Journal of Fluid Mechanics*, 37 (4), 643-655.
50. Wu, J., 1973. Wind-induced turbulent entrainment across a stable density interface. *Journal of Fluid Mechanics*, 61(2), 275-287.
51. Cai, J., Jo, B., Erkan, N., Okamoto, K., 2016. Effect of non-condensable gas on thermal stratification and flow patterns in suppression pool. *Nuclear Engineering and Design*, 300, 117-126.
52. Chen, M.H., Cardoso, S.S.S., 2000. The mixing of liquids by a plume of low-Reynolds number bubbles. *Chemical Engineering Science*, 55 (14), 2585-2594.
53. Tang, J., Yan, C., Sun, L., 2015. A study visualizing the collapse of vapor bubbles in a subcooled pool. *International Journal of Heat and Mass Transfer*, 88, 597-608.
54. Fukuda, S., 1982. Pressure Variations due to Vapor Condensation in Liquid, (II). *Journal of the Atomic Energy Society of Japan*, 24 (6), 466-474.
55. Ko, N.W.M., Lau, K.K., 1989. Flow structures in initial region of two interacting parallel plane jets. *Experimental Thermal and Fluid Science*, 2 (4), 431-449.
56. Choo, Y.J., Song, C.H., 2010. PIV measurements of turbulent jet and pool mixing produced by a steam jet discharge in a subcooled pool. *Nuclear Engineering and Design*, 240 (9), 2215-2224.
57. Pope, S.B., 2000. *Turbulent Flow*. First ed., Cambridge University Press, Section 5.1.
58. Hussein, H.J., Capp, S.P., George, W.K., 1994. Velocity measurements in a high Reynolds number, momentum-conserving, axisymmetric, turbulent jet. *Journal of Fluid Mechanics*, 258, 31-75.
59. Van Wissen, R.J.E., Schreel, K.R.A.M., Van Der Geld, C.W.M., 2005. Particle image velocimetry measurements of a steam-driven confined turbulent water jet. *Journal of Fluid Mechanics*, 530, 353-368.
60. Malavasi, S., Messaa, G., Fratino, U., Pagano, A., 2012. On the pressure losses through perforated plates. *Flow Measurement and Instrumentation*, 28, 57-66.
61. Cho, S., Chun, S.Y., Baek, W.P., Kim, Y., 2004. Effect of multiple holes on the performance of sparger during direct contact condensation. *Experimental Thermal and Fluid Science*, 28 (6), 629-638.
62. Kayser, J.C., Shambaugh, R.L., 1991. Discharge coefficients for compressible flow through small-diameter orifices and convergent nozzles. *Chemical Engineering Science*, 46 (7), 1697-1711.